Supporting Information for "Disentangling Carbon Concentration Changes Along Pathways of North Atlantic Subtropical Mode Water"

Daan Reijnders[1], Dorothee C. E. Bakker[2], Erik van Sebille[1]

[1]Institute for Marine and Atmospheric research Utrecht, Utrecht University, Utrecht, the Netherlands

[2]Centre for Ocean and Atmospheric Sciences, School of Environmental Sciences, University of East Anglia, Norwich, United Kingdom

Contents of this file

Text S1. Model–Observation Comparison

To compare the FREEGLORYS2V4 and FREEBIORYS2V4 products to observations, we compare modeled temperature, salinity, temperature stratification and DIC concentrations to observed bottle (DIC) and CTD (temperature, salinity and temperature stratification) data from the WOCE/CLIVAR A20 section along ∼52°W (see Figure S1). This

approach is similar to that of Kwon, Park, Gary, and Lozier (2015). These observational data come from three cruises across two decades: in 1997 (Pickard, 2022), 2003 (Toole & MacDonald, 2022), and 2012 (Swift et al., 2022). In this section, we also compare locations of modeled and observed NASTMW. The criteria used to define modeled NASTMW are partly motivated by these findings, as well as on the sensitivity analysis in Text S2.

We focus on the region between 15°N to 40°N, considering depths up to 600 m. Figures S2, S3, and S4 show model-observation comparisons for temperature, salinity and temperature stratification for A20 sections in 1997, 2003, and 2012 respectively. Here we also indicate NASTMW using a temperature and stratification constraint (see section 2.2 of the main text for the definition used in the rest of this study). Model NASTMW is indicated by $17\,^{\circ}\mathrm{C} < T < 20.5\,^{\circ}\mathrm{C}$ and $\partial T/\partial z < 0.01\,^{\circ}\mathrm{C\,m^{-1}}$. Observed NASTMW follows a slightly stricter typical definition of $17\,^{\circ}\mathrm{C} < T < 19\,^{\circ}\mathrm{C}$ and $\partial T/\partial z < 0.01\,^{\circ}\mathrm{C\,m^{-1}}$. Here the maximum stratification criterion for observations is somewhat increased, and thus 'relaxed', with respect to the weaker maximum stratification of $0.006\,^{\circ}\mathrm{C\,m^{-1}}$ used by Kwon et al. (2015). This is because with $0.006\,^{\circ}\mathrm{C\,m^{-1}}$ we barely detected NASTMW for observations in 2003 and 2012. We apply a 20 m rolling mean to the observed temperature stratification to smooth out small measurement errors.

As can be seen, the model includes NASTMW with a typical minimum in temperature stratification. Overall, model temperature biases are reasonably small, with slightly positive biases north of 30°N and negative biases south of this latitude. Salinity biases in the observed NASTMW region are generally negative. The model also exhibits a higher temperature stratification in the observed NASTMW region. Stratification minima coinciding with NASTMW are at slightly shallower depths. Note that the observed NASTMW here

exhibits a wedge-like structure. The warm bias south of 30°N and higher temperature stratification are the main motivations for relaxing the temperature and stratification constraints in the model NASTMW definition. In Figure S2a & g, a cool bias in the region of low stratification would suggest that including temperature above 16 or 16.5 °C would better capture NASTMW in the model. However, in Figures S3a & g and Figures S4a & g, the 16–17 °C range is not included in the low stratification zone, while the range 19–20 °C is, coinciding with the model warm bias. Our choice to define the temperature range of 17–20.5 °C is a trade off in choosing a relaxed temperature range that will most often coincide with low-stratification criterion, while ensuring the temperature range stays small enough to represent a homogeneous water mass. This is further motivated by the sensitivity analysis in Text S2. Overall, this yields realistic NASTMW volumes, thicknesses and spatial extents.

We also compare modeled temperature and NASTMW with data from the World Ocean Atlas 2023 (WOA23; Reagan & NOAA National Centers for Environmental Information, 2023). We compute a model climatology for March and September between the years 1995 and 2017 – the model years used in this study. We compare this to the WOA23 climatology at 1/4° resolution, produced for the years 1991-2020. Figure S5 shows model temperature biases at 5, 200, and 500 m depths. It can readily be seen that the model does not correctly reproduce the Gulf Stream separation around Cape Hatteras, leading to a warm bias near the coastline further north. This is a known issue in ocean modeling (Bryan et al., 2007; Chassignet & Marshall, 2008). This also manifests itself in a model cold bias around 500 m depth just south of the modeled Gulf stream. In the Sargasso Sea, temperature biases are slightly positive at 200 m depth and become slightly negative at

500 m. This indicates a bias towards an increased temperature stratification, as was also found in the WOCE transects.

Additionally, the model exhibits an overall negative salinity bias in the region, which is especially pronounced in the surface layer (Fig. S6). Negative surface salinity biases are more commonly observed in coarse climate models (Flato et al., 2013; Park et al., 2016). A fresher upper ocean may lead to decreased DIC concentrations, because freshwater input can locally dilute the DIC pool. Since we are interested in how mixing influences DIC concentrations, we do not apply salinity corrections in our main analyses (see section 2.5 in the main text), yet such a correction is warranted when comparing DIC concentrations between the model and observations.

To further investigate how the location of modeled NASTMW may differ from observations, we plot the location of the climatological mixed layer depth (MLD) in March in Figure S7. Observations here are taken from WOA18 (Boyer et al., 2018). Regions of deep mixed layers in the northern part of the Sargasso Sea are possible NASTMW formation regions. As can be seen, the modeled mixed layer maximum in the Sargasso Sea is shallower than in observations. This is in line with the higher temperature stratification found in the previous model-observation comparisons. We expect model NASTMW to be mainly produced in the region of the 250-300 m maximum between 65°W and 50°W. In observations, mixed layer maxima around this depth extend further West, up to 70°W.

In Figure S8, we compare the climatological location of NASTMW in our model data (1995-2017) with climatological NASTMW in WOA23 (1991-2020). For WOA23 (S8a & b), we again use the NASTMW criterion of $17\,^{\circ}\mathrm{C} < T < 19\,^{\circ}\mathrm{C}$ and $\partial T/\partial z < 0.01\,^{\circ}\mathrm{C\,m^{-1}}$. For the model, we use the adjusted temperature criterion of $17\,^{\circ}\mathrm{C} < T < 20.5\,^{\circ}\mathrm{C}$, applied

to the climatological temperature (S8c & d) and applied to daily temperature fields, after which a climatological NASTMW is computed (S8e & f). In this case, we do not use any constraints for contiguity or specific layer thickness, but do cut off NASTMW at 35°W to exclude Madeira mode water (see main text section 2.2). The spatial distribution of NASTMW thickness computed from model climatological temperatures and computed from daily values here broadly agree, so we will use the NASTMW computed from the WOA temperature climatology as a proxy for a climatology of NASTMW itself. First, we can see that the model NASTMW has a core that is located more eastward, especially in September. In both the model and WOA case, the core is located south of the March MLD maximum (see Figure S7a). Latitudinal extents of model and WOA NASTMW agree. The NASTMW computed from WOA is thicker, which again can be explained through the increased stratification in the model.

In summary, the FREEGLORYS2V4 NASTMW is produced through convective events associated with shallower MLD maxima and a slightly stronger vertical temperature stratification. This causes the modeled NASTMW to be thinner. The strong winter convection and NASTMW production site is located further eastward in comparison to observations. While ideally the locations between modeled and observed NASTMW would match, we still use the modeled NASTMW for a process-level understanding of how DIC concentrations change along NASTMW pathways.

Lastly, we compare modeled DIC in FREEBIORYS2V4 to observed DIC concentrations using bottle data from the three A20 cruises, shown in Figure S9. Here, we also show salinity-normalized values of DIC (nDIC, normalized to a typical value of 36 psu). Quality-controlled bottle DIC values are converted from molality ($\mu mol\,kg^{-1}$) to molar

concentrations ($\mu mol\,L^{-1}$), as used in this study. For this we use CTD temperatures and salinities in conjunction with the Thermodynamic Equation of Seawater 2010 (TEOS-10; McDougall & Barker, 2011). Note that the model and observations are both subject to variations of DIC concentrations at fixed positions, due to internal variability. We therefore do not expect modeled concentrations to match one-on-one with observations. Instead, we are interested in the general distribution of DIC concentrations. While in 1997, there is good agreement of modeled and observed DIC concentration in the NASTMW region, observed DIC is higher in subsequent years. The salinity normalization causes an overall better agreement between the model and observations taken in 2003 and 2012, as well as for the upper 200 meters in 1997. Overall, the vertical structure of increasing (n)DIC with depth is captured. Figure S10 compares the bottle and observed DIC values. While the mean DIC bias in 1997 is almost equal to a typical measurement precision of $\sim 1\,\mu mol\,L^{-1}$ (Sarmiento & Gruber, 2006), the bias between bottle and modeled DIC becomes more negative over time, while the Pearson correlation coefficient remains steady at 0.92. This increase in model bias is partially due to the model salinity bias. Figure S11 shows a bottle-model comparison for nDIC. Figure S11a–c shows a smaller overall negative bias for 2003 and 2012, while the bias for 1997 becomes positive. The distribution shows a wider spread for nDIC than for DIC (Fig. S10), meaning that salinity correction can lead to larger outliers due to bias multiplication when salinity and DIC biases have different causes. The linear regressions for nDIC (Fig. S11d–f) all have slopes smaller than 1, showing a model underestimation for high nDIC, while the overall correlation remains high with the Pearson-R ranging between 0.91-0.93. In the case of both DIC and nDIC, the model bias becomes more negative over time.

To further illustrate how FREEBIORYS2V4 responds to the prescribed increase of atmospheric pCO_2, Figure S12a shows the trend of DIC concentrations at 10 m depth. Trends are computed between 1995 and 2017 by applying an seasonal decomposition based on moving averages, followed by a linear regression. This shows an overall decrease in upper-ocean DIC, with a trend between 0 and -1 µmol/L/year in most of the Sargasso Sea. However, Figure S12b & c show that this is due to a modeled salinity decrease. Adjusting for this, the nDIC trend becomes positive in the Sargasso Sea and exhibits pronounced spatial variability.

Between 1988 and 2011, seasonally-detrended nDIC observations show a trend of $+1.08 \pm 0.05$ µmol/kg/year at the Bermuda Atlantic Time-series Study (BATS) site at 31°40′ N, 64°10′ W and Hydrostation S at 32°10′N, 64°10′W (Bates et al., 2012). Figure S12d shows a time series of model nDIC near the BATS site at 10 m depth, which exhibits a much smaller deseasonalized trend of 0.2 µmol/L/yr, while exhibiting notable interannual variability. Since the model's nDIC response to increasing atmospheric pCO_2 in the Sargasso Sea is about a factor 5 weaker than observed, our dataset is not suitable for investigating changes in carbon fluctuations along NASTMW pathways due to rising anthropogenic carbon emissions. Instead, we apply a process-based view that takes into account interannual variability without focusing on trends.

Text S2. NASTMW Definition Sensitivity Analysis

We test the sensitivity of the modeled NASTMW in March and September to the following changes:

1. Lowering the maximum temperature stratification criterion, comparing $0.01\,^{\circ}\mathrm{C\,m^{-1}}$ and $0.006\,^{\circ}\mathrm{C\,m^{-1}}$.

2. Varying the maximum temperature criterion, comparing 19 °C, 20 °C, 20.5 °C and 21 °C. The lowest value in this range is typical in literature (Kwon & Riser, 2004; Joyce et al., 2013), while 20 °C has been used in the modeling study by Kwon et al. (2015). The highest two values are included due to the model's warm bias in certain regions, discussed in Text S1.

3. Lowering the minimum temperature criterion, comparing 17 °C and 16.5 °C, motivated by the model's cold bias in certain regions, discussed in Text S1.

Since it is computationally expensive to compute climatologies of NASTMW for each of these combinations, we instead apply these criteria to climatologies of the model temperature for March and September (1995-2017). The results are shown in Figure S13. As in Figure S8, we do not consider individual layer thickness or contiguity here. It can immediately be seen that a maximum stratification criterion of $0.006\,^{\circ}\mathrm{C\,m^{-1}}$ yields NASTMW that is too thin, when compared to observed core thickness of around 300–400 m in the literature (Kwon & Riser, 2004; Fratantoni et al., 2013; Billheimer & Talley, 2016). This emphasizes the need to increase the maximum stratification criterion to $0.01\,^{\circ}\mathrm{C\,m^{-1}}$. The effect of increasing the upper temperature boundary can be seen as the NASTMW region increases towards the south-west. This means that the temperature criterion provides the main limiting factor for being defined as NASTMW in this southwestern sector. The difference between the lower temperature boundaries of 16.5 °C and 17 °C is rather small, as is the difference between the upper boundaries 20.5 °C and 21 °C. The temperature range of $17\,^{\circ}\mathrm{C} < T < 20.5\,^{\circ}\mathrm{C}$ indeed seems a good trade-off between often coinciding with the low-stratification region, while at the same time keeping the total temperature range somewhat limited to reflect the homogeneity of NASTMW.

The contiguity and individual layer thickness constraints, as discussed in Section 2.2 in the main text, also affect the total NASTMW volume. To test the sensitivity of the NASTMW volume to these constrains, we compute the volume using only the temperature and stratification criteria and compare this to the volume when adding the thickness and contiguity criteria. Figure S14 shows that the volume experiences a pronounced seasonal cycle. The average yearly minimum volume is $4.1 \times 10^{14}\,\mathrm{m}^3$, while the average yearly maximum is $9.0 \times 10^{14}\,\mathrm{m}^3$. This is close to the value of $9.1 \times 10^{14}\,\mathrm{m}^3$ found by Joyce (2012) using a temperature and salinity constraint. The seasonal NASTMW production of $4.9 \times 10^{14}\,\mathrm{m}^3$ is higher than the $2.7 \times 10^{14}\,\mathrm{m}^3$ (8.6 Svy, where $1\,\mathrm{Svy} \approx 3.15 \times 10^{13}\,\mathrm{m}^3$) found by Forget, Maze, Buckley, and Marshall (2011), which was found without a stratification constraint. When that constraint is absent, NASTMW production and destruction happens mostly through cooling and warming due to air-sea heat fluxes and vertical mixing, while the pronounced seasonal effects of stratification creation and destruction are ignored. In general, NASTMW volumes are highly sensitive to the criteria used (Joyce, 2012). Note, however, that the added thickness and contiguity criteria can help us eliminate small, spurious NASTMW volumes, without changing the total volume much when compared to the seasonal cycle.

Text S3. Subduction at Longer Integration Times

In the main text, we discussed NASTMW parcels that subducted within the previous year. Here we investigate the effect of including NASTMW parcels that have subducted from the mixed layer on September 1st over the course of two (Figs. S15 & S16), and three years (Figs. S17 & S18), such that they end up in NASMTW again at September 1st. In both cases, the order of magnitude of the total ΔDIC is similar to that of sub-

duction over the course of one year (110 µmol L^{-1} for two and three years, compared to 101 µmol L^{-1} for one year). While we see an increase in the contribution of soft-tissue, carbonate and residual fluxes, mixing fluxes are still dominant in setting the DIC concentration. This suggests that also at larger time scales, adjustment to the ambient water column condition is the main determinant for setting DIC concentrations of subducting NASTMW parcels. However, the increased contribution of biogeochemical fluxes indicates that the parcel's DIC concentrations are to a larger extent influenced directly by soft-tissue remineralization, which shapes the ambient vertical structure of DIC in the water column.

The distribution of total ΔDIC (Figs. S15a & S17a) has a tail that extends to larger extremes than during subduction over 1 year (Fig. 4 in the main text). When considering longer subduction timescales, backward-tracked parcels can come from a much larger region. Parcels in the right tail of the distribution are found to come from areas where mixed-layer DIC concentrations are generally lower, including for example the Carribean Sea.

Looking at the timescales of enrichment and depletion regimes (Figs. S16 & S18), we notice that distributions of regime timescales are similar, although with a thinner tail at longer timescales: as subduction occurs over longer timescales, downwelling and the associated steady increase of DIC can be more variable as the parcel travels from the mixed layer to NASTMW. This causes longer periods of enrichment to be more easily interspersed by depletion.

Text S4. Sensitivity of $\Delta\rho$ for Export Pathways

Figures S19 – S22 show the results for exported parcels, where we use $\Delta\sigma = 0\,\mathrm{kg\,m^{-3}}$ and $0.05\,\mathrm{kg\,m^{-3}}$ instead of $\Delta\sigma = 0.01\,\mathrm{kg\,m^{-3}}$ as used in the main text. When we lower $\Delta\sigma$ to $0\,\mathrm{kg\,m^{-3}}$, the number of parcels that are considered exported is reduced by about a factor 3 (from 15.3% to 4.7% of all parcels). When increasing $\Delta\sigma$ to $0.05\,\mathrm{kg\,m^{-3}}$, the number of parcels doubles to 30.6%. However, the distribution and mean of ΔDIC in both cases remains approximately equal to that found for $\Delta\sigma = 0.01\,\mathrm{kg\,m^{-3}}$ (comparing Figures S19a-c and S21a-c to Figure 9a-c from the main text). This is also the case for the timescale distribution and magnitudes (comparing Figures S20 and S22 to Figure 10 in the main text. The monthly fluxes exhibit similar patterns, although vary in magnitude, with the flux ranges generally being stronger given stricter criteria (Figures S19d-f and S21d-f to Figure 9d-f from the main text). However, since the residual contributes significantly more to ΔDIC in the export pathways than for the other NASMTW pathways, the flux disentanglement into its components is less well-constrained.

Text S5. Varying Smoothing Window Widths

The width of the window by which we smooth our DIC anomaly timeseries will influence the timescales of the regimes that we detect using the method presented in section 2.6 of the main text. After all, smoothing will filter out minor fluctuations in the DIC anomaly, such that, if they are small in magnitude, brief periods of enrichment and depletion are smoothed out. Inherently, the smoothing window width thus influences the timescale distributions that we find. In the main text, we focus on a window width of ten days. Here, we show regime timescale results when we identify regimes without smoothing, as well as by applying a smoothing window of 6 and 20 days.

The results without smoothing are found in Fig. S23 (subduction), S24 (persistence), S25 (ventilation), and S26 (export). In each of the cases, we see that the distribution of depletion and enrichment timescales is largely concentrated at timescales of 10 days or less. The partitioning of flux contributions to events, however, remains roughly similar at each timescale. For subduction, persistence, and export, we no longer see a net depletion at any timescale. In the case of a 10-day smoothing window, short depletion events would be interspersed with longer enrichment, causing net depletion for short scales (below 10 to 40 days, depending on the pathway), and enrichment at longer scales. Without smoothing, brief small depletion events are included that could be smoothed out for longer timescales. These brief depletion events can break up a steady background enrichment that would have been identified if timescale smoothing was applied. This thus serves to illustrate how smoothing acts as a lens by which small, brief fluctuations, which may be due to numerical noise, are ignored.

The results with 6-day smoothing are found in Fig. S27 (subduction), S28 (persistence), S29 (ventilation), S30 (export), while the results using a 20-day smoothing window are found in Fig. S31 (subduction), S32 (persistence), S33 (ventilation), S34 (export). When comparing these timescale distributions to those found using a 10-day smoothing window in the main text, we see that generally speaking, the distributions are qualitatively similar, but with their modes and tails shifted towards longer timescales. This further illustrates how the smoothing window simply acts as a lens by which short-term fluctations can be filtered out.

References

Bates, N. R., Best, M. H. P., Neely, K., Garley, R., Dickson, A. G., & Johnson, R. J.

(2012). Detecting anthropogenic carbon dioxide uptake and ocean acidification in the North Atlantic Ocean. *Biogeosciences*, *9*(7), 2509–2522. doi: 10.5194/bg-9-2509-2012

Billheimer, S., & Talley, L. D. (2016). Annual cycle and destruction of eighteen degree water. *Journal of Geophysical Research: Oceans*, *121*(9), 6604–6617. doi: 10.1002/2016JC011799

Boyer, T. P., García, H. E., Locarnini, R. A., Zweng, M. M., Mishonov, A. V., Reagan, J. R., ... Smolyar, I. V. (2018). *[Dataset] World Ocean Atlas 2018, Mixed Layer Depth - statistical mean on 1/4° grid for 2005-2017.* NOAA National Centers for Environmental Information. Retrieved from `https://www.ncei.noaa.gov/archive/accession/NCEI-WOA18` (Accesed on 1 March 2023)

Bryan, F. O., Hecht, M. W., & Smith, R. D. (2007). Resolution convergence and sensitivity studies with North Atlantic circulation models. Part I: The western boundary current system. *Ocean Modelling*, *16*(3-4), 141–159. doi: 10.1016/j.ocemod.2006.08.005

Chassignet, E. P., & Marshall, D. P. (2008). Gulf Stream separation in numerical ocean models. In M. W. Hecht & H. Hasumi (Eds.), *Geophysical Monograph Series* (Vol. 177, pp. 39–61). Washington, D. C.: American Geophysical Union. doi: 10.1029/177GM05

Flato, G., Marotzke, J., Abiodun, B., Braconnot, P., Chou, S., Collins, W., ... Rummukainen, M. (2013). Evaluation of climate models. In T. Stocker et al. (Eds.), *Climate change 2013: The physical science basis. contribution of Working Group I to the fifth assessment report of the Intergovernmental Panel on Climate Change.* Cambridge, United Kingdom and New York, NY, USA: Cambridge Uni-

versity Press. Retrieved from https://doi.org/10.1017/CBO9781107415324 doi: 10.1017/CBO9781107415324

Forget, G., Maze, G., Buckley, M., & Marshall, J. (2011). Estimated Seasonal Cycle of North Atlantic Eighteen Degree Water Volume. *Journal of Physical Oceanography*, *41*(2), 269–286. doi: 10.1175/2010JPO4257.1

Fratantoni, D. M., Kwon, Y.-O., & Hodges, B. A. (2013). Direct observation of subtropical mode water circulation in the western North Atlantic Ocean. *Deep Sea Research Part II: Topical Studies in Oceanography*, *91*, 35–56. doi: 10.1016/j.dsr2.2013.02.027

Joyce, T. M. (2012). New perspectives on Eighteen-Degree Water formation in the North Atlantic. *Journal of Oceanography*, *68*(1), 45–52. doi: 10.1007/s10872-011-0029-0

Joyce, T. M., Thomas, L. N., Dewar, W. K., & Girton, J. B. (2013). Eighteen Degree Water formation within the Gulf Stream during CLIMODE. *Deep Sea Research Part II: Topical Studies in Oceanography*, *91*, 1–10. doi: 10.1016/j.dsr2.2013.02.019

Kwon, Y.-O., Park, J.-J., Gary, S. F., & Lozier, M. S. (2015). Year-to-year reoutcropping of Eighteen Degree Water in an eddy-resolving ocean simulation. *Journal of Physical Oceanography*, *45*(4), 1189–1204. doi: 10.1175/JPO-D-14-0122.1

Kwon, Y.-O., & Riser, S. C. (2004). North Atlantic Subtropical Mode Water: A history of ocean-atmosphere interaction 1961–2000. *Geophysical Research Letters*, *31*(19), L19307. doi: 10.1029/2004GL021116

McDougall, T. J., & Barker, P. M. (2011). *Getting started with TEOS-10 and the Gibbs Seawater (GSW) Oceanographic Toolbox*. SCOR/IAPSO WG127.

Park, T., Park, W., & Latif, M. (2016). Correcting North Atlantic sea surface

salinity biases in the Kiel Climate Model: Influences on ocean circulation and Atlantic Multidecadal Variability. *Climate Dynamics*, *47*(7-8), 2543–2560. doi: 10.1007/s00382-016-2982-1

Pickard, R. (2022). *[Dataset] CTD and DIC bottle data from Cruise 316N151_3, WHP netCDF.* Version: WHP netCDF. CCHDO. Retrieved from `https://cchdo.ucsd.edu/cruise/316N151_3` (Accesed on 1 March 2023)

Reagan, J. R., & NOAA National Centers for Environmental Information. (2023). *[Dataset] World Ocean Atlas 2023, NCEI Accession 0282728, Temperature - statistical mean on 1/4° grid for 1991-2020.* NOAA National Centers for Environmental Information. Retrieved from `https://www.ncei.noaa.gov/archive/accession/0282728` (Accesed on 1 March 2023)

Sarmiento, J. L., & Gruber, N. (2006). *Ocean biogeochemical dynamics.* Princeton: Princeton university press.

Swift, J., Feely, R., & Wanninkhof, R. (2022). *[Dataset] CTD and DIC bottle data from Cruise 33AT20120419, WHP netCDF.* Version: WHP netCDF. CCHDO. Retrieved from `https://cchdo.ucsd.edu/cruise/33AT20120419` (Accesed on 1 March 2023)

Toole, J., & MacDonald, A. (2022). *[Dataset] CTD and DIC bottle data from Cruise 316N200309, WHP netCDF.* Version: WHP netCDF. CCHDO. Retrieved from `https://cchdo.ucsd.edu/cruise/316N200309` (Accesed on 1 March 2023)

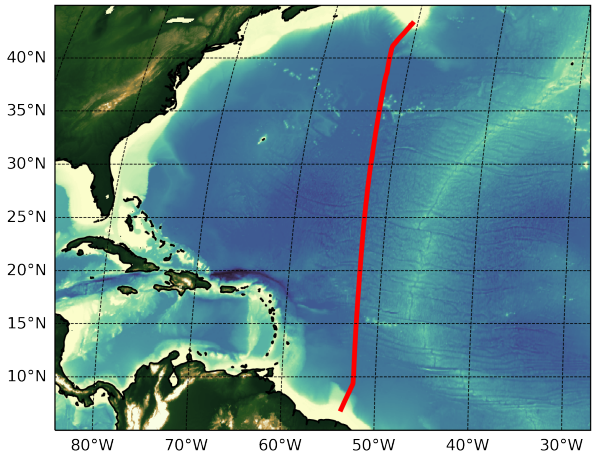

Figure S1. WOCE A20 section, used to compare CTD and bottle data with FREE-GLORYS2V4 (temperature, stratification, and salinity) and FREEBIORYS2V4 (DIC).

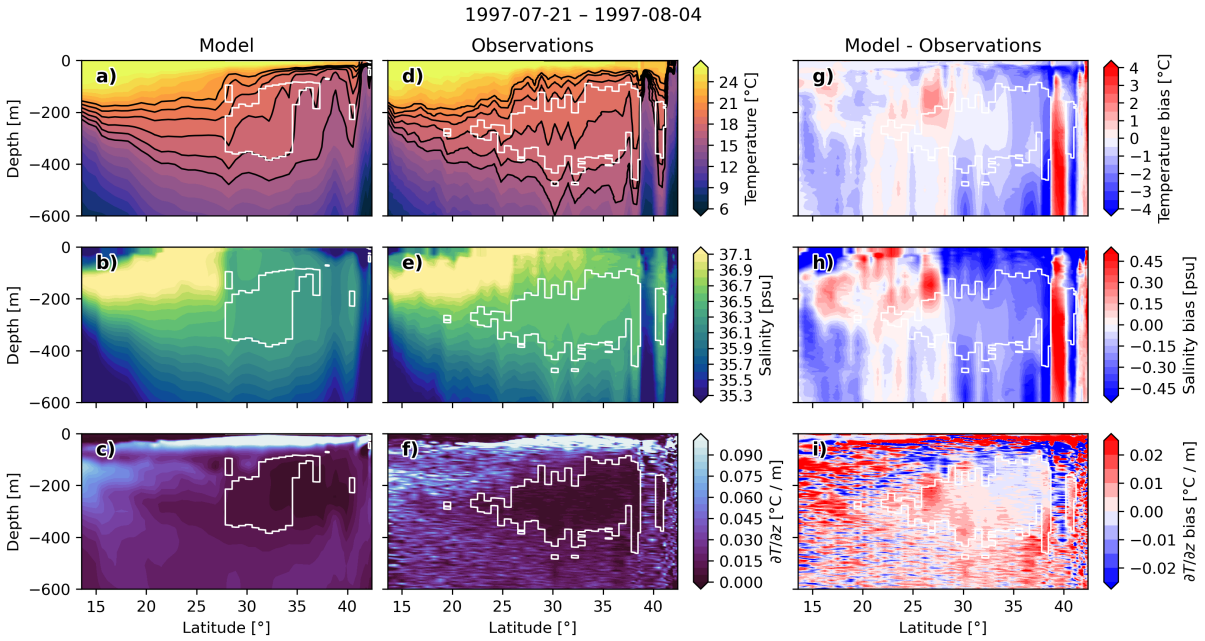

Figure S2. Model–observation comparison along the WOCE A20 section in 1997 at ∼ 52°W (Pickard, 2022). (a) Model temperature (b) salinity, and (c) temperature stratification snapshots are for 28 July 1997. White contours indicate modeled NASTMW based on temperature and stratification criteria. (d–f) show observed temperature, salinity and stratification at the corresponding observations along A20 between 21 Jul - 14 Aug 1997. Black lines in (a) and (d) indicate $16-21\,^{\circ}\mathrm{C}$ isotherms. (g–i) show the model bias (model - observations, with the NASTMW constraints from observations).

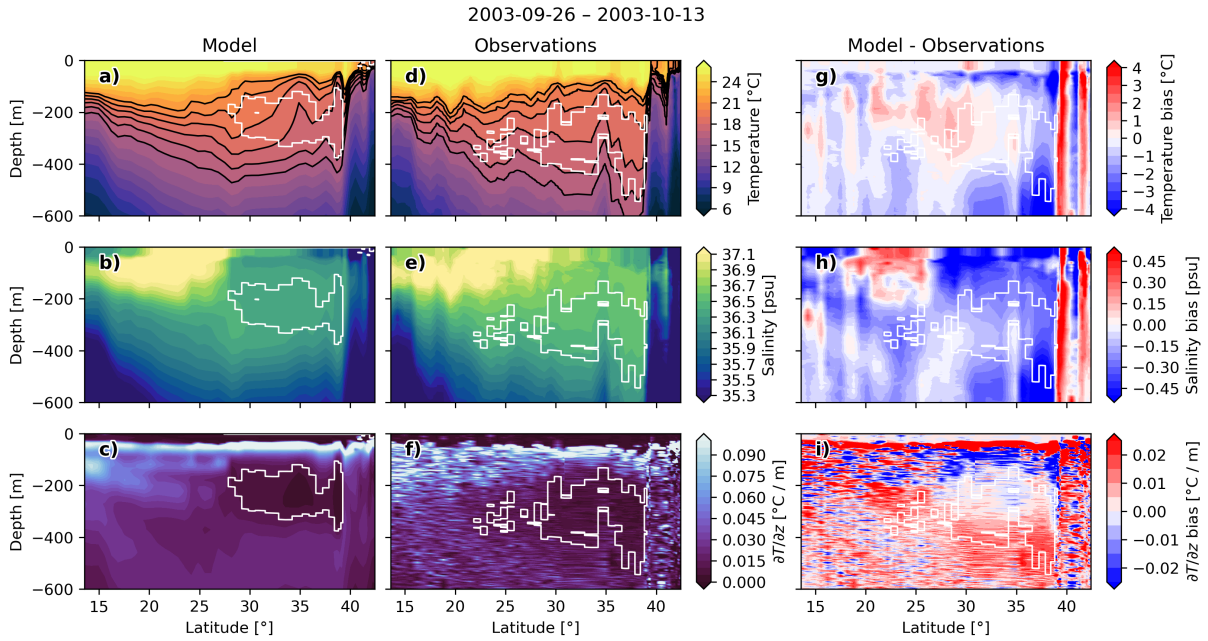

Figure S3. Similar to Figure S2, but for the CLIVAR A20 section in 2003 (Toole & MacDonald, 2022). Model sections (a–c) are taken at 3 October 2003. Observations (d–f) are taken between 26 September – 13 October 2003.

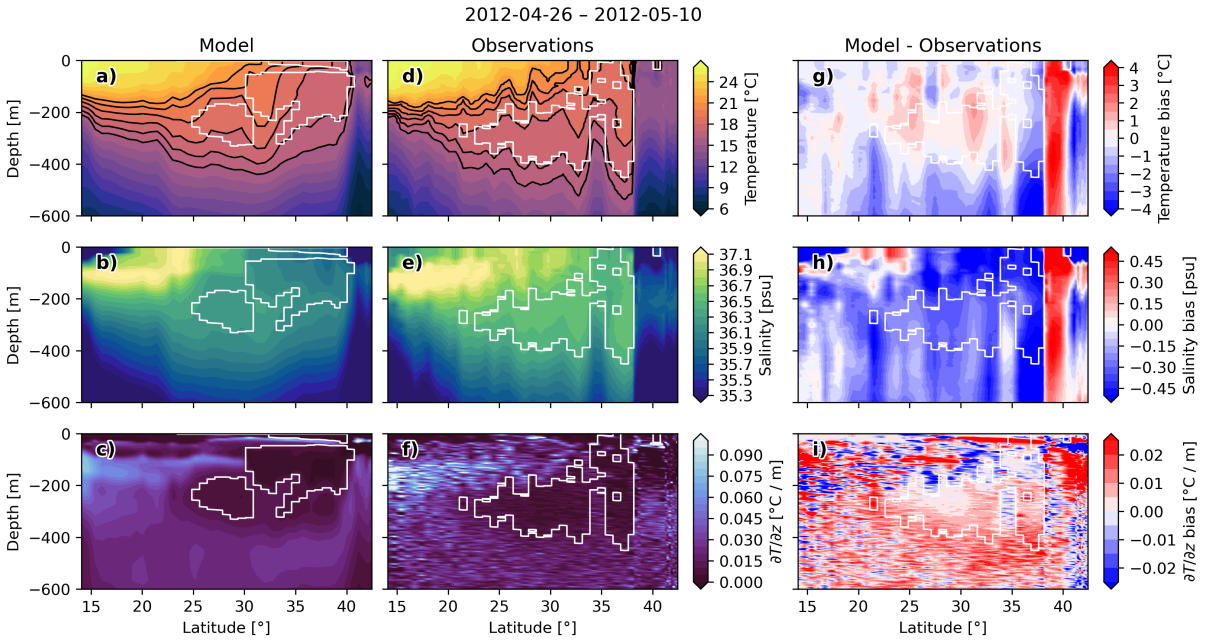

Figure S4. Similar to Figure S2, but for the CLIVAR A20 section in 2012 (Swift et al., 2022). Model sections (a–c) are taken at 2 May 2012. Observations (d–f) are taken between 26 April – 10 May 2012.

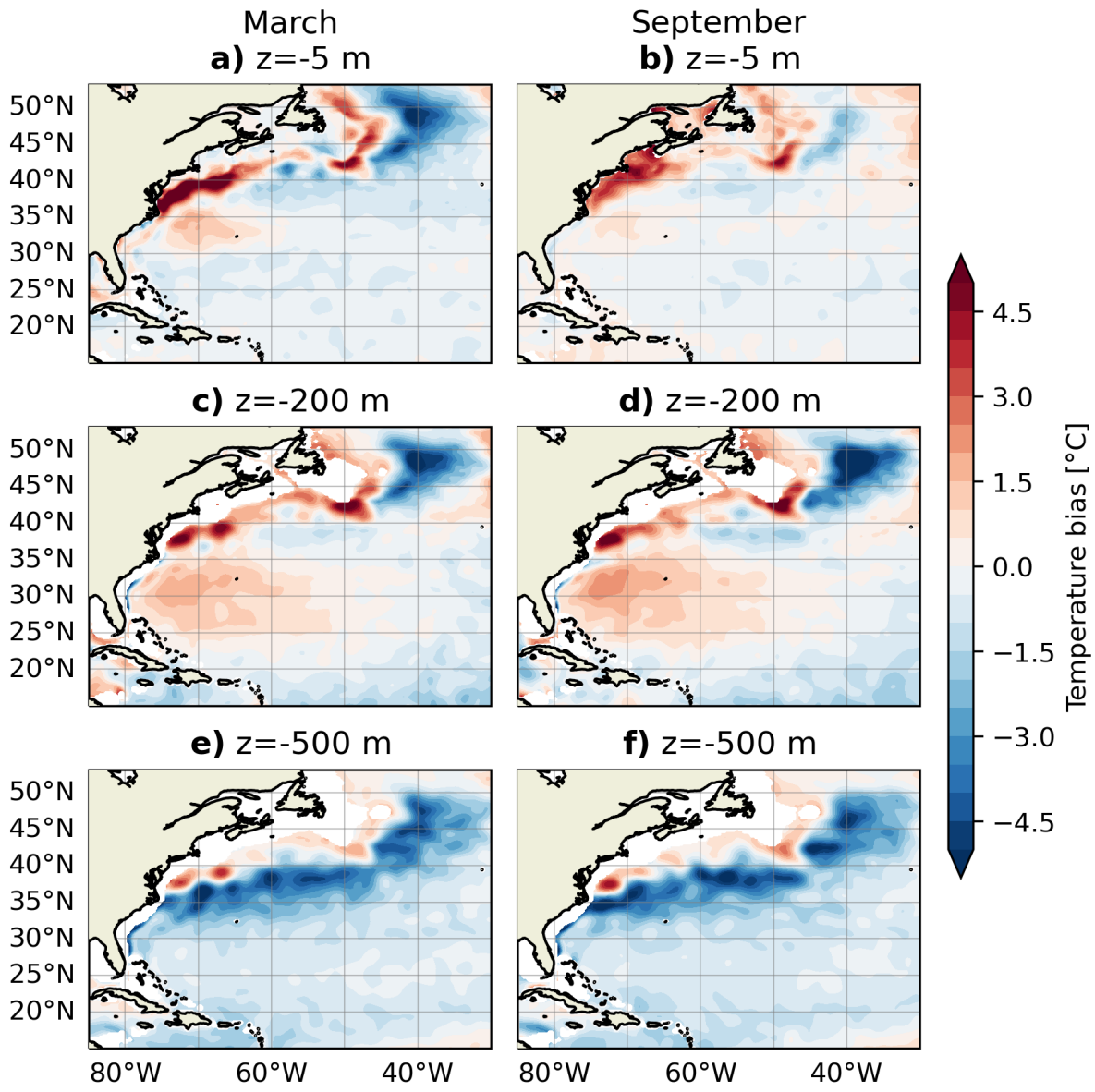

Figure S5. Model temperature bias. Computed by subtracting WOA23 climatological temperatures (1991–2020) from model temperature climatology (1995–2017).

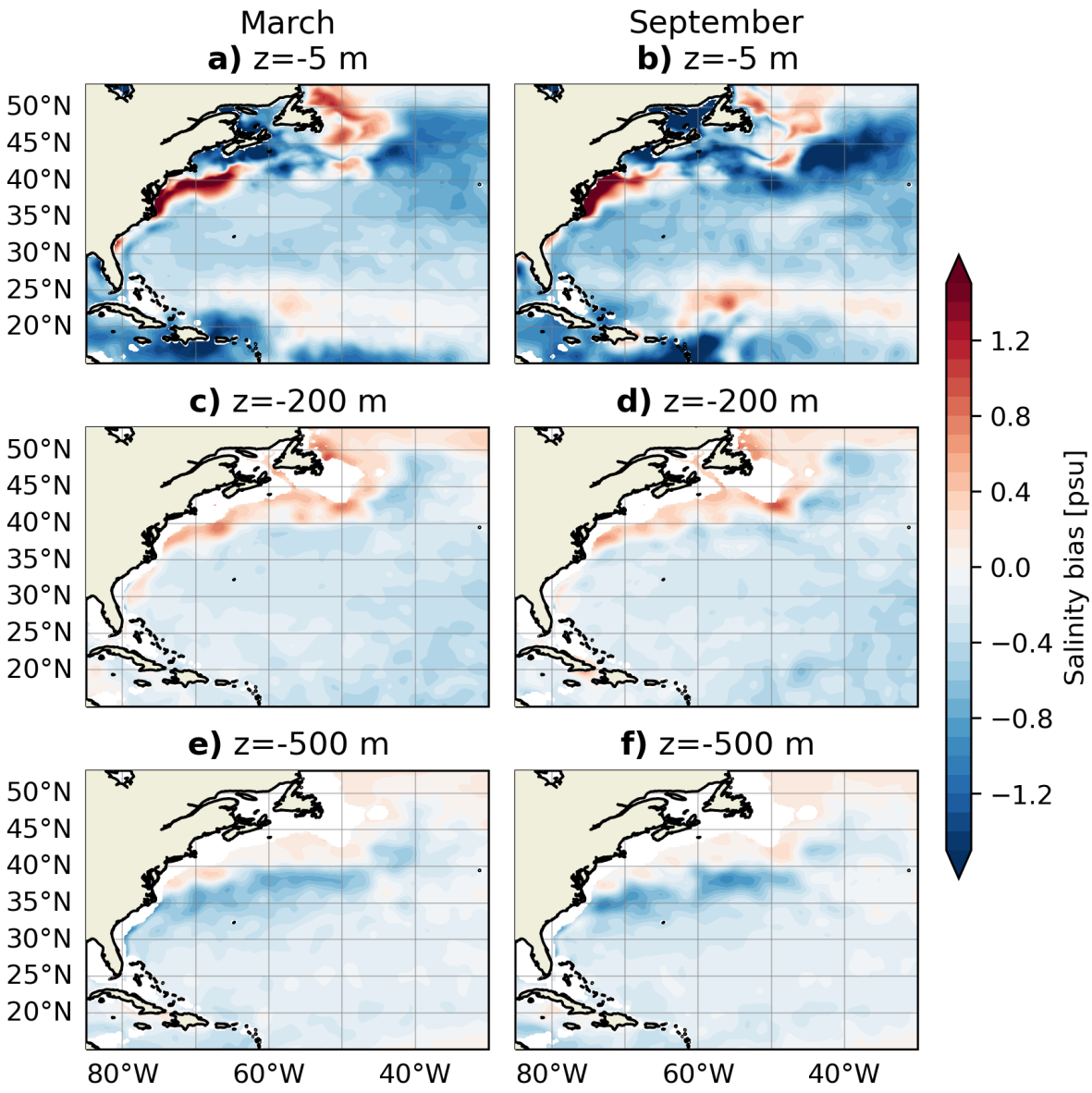

Figure S6. Model salinity bias. Computed by subtracting WOA23 climatological salinities (1991–2020) from model salinity climatology (1995–2017).

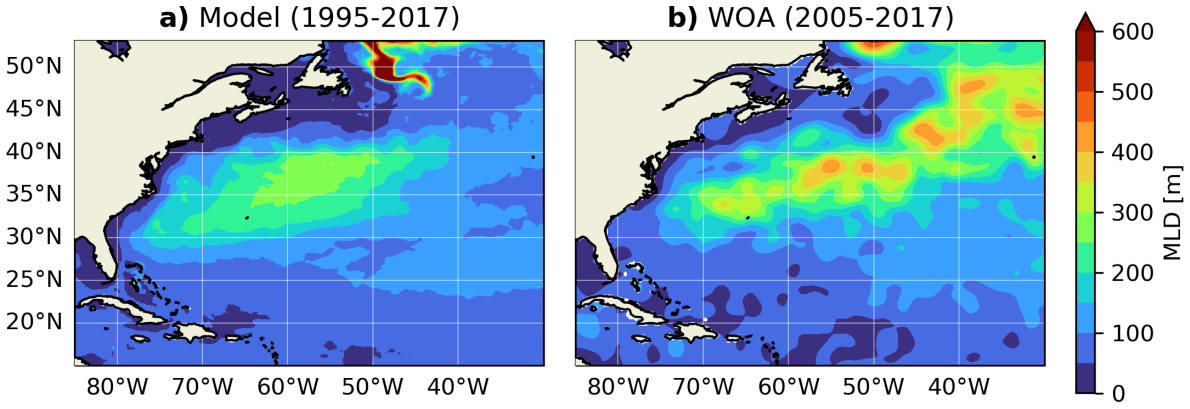

Figure S7. Climatological mixed layer depths from (a) FREEGLORYS2V4 (1995-2017) and (b) WOA18 (2005-2017).

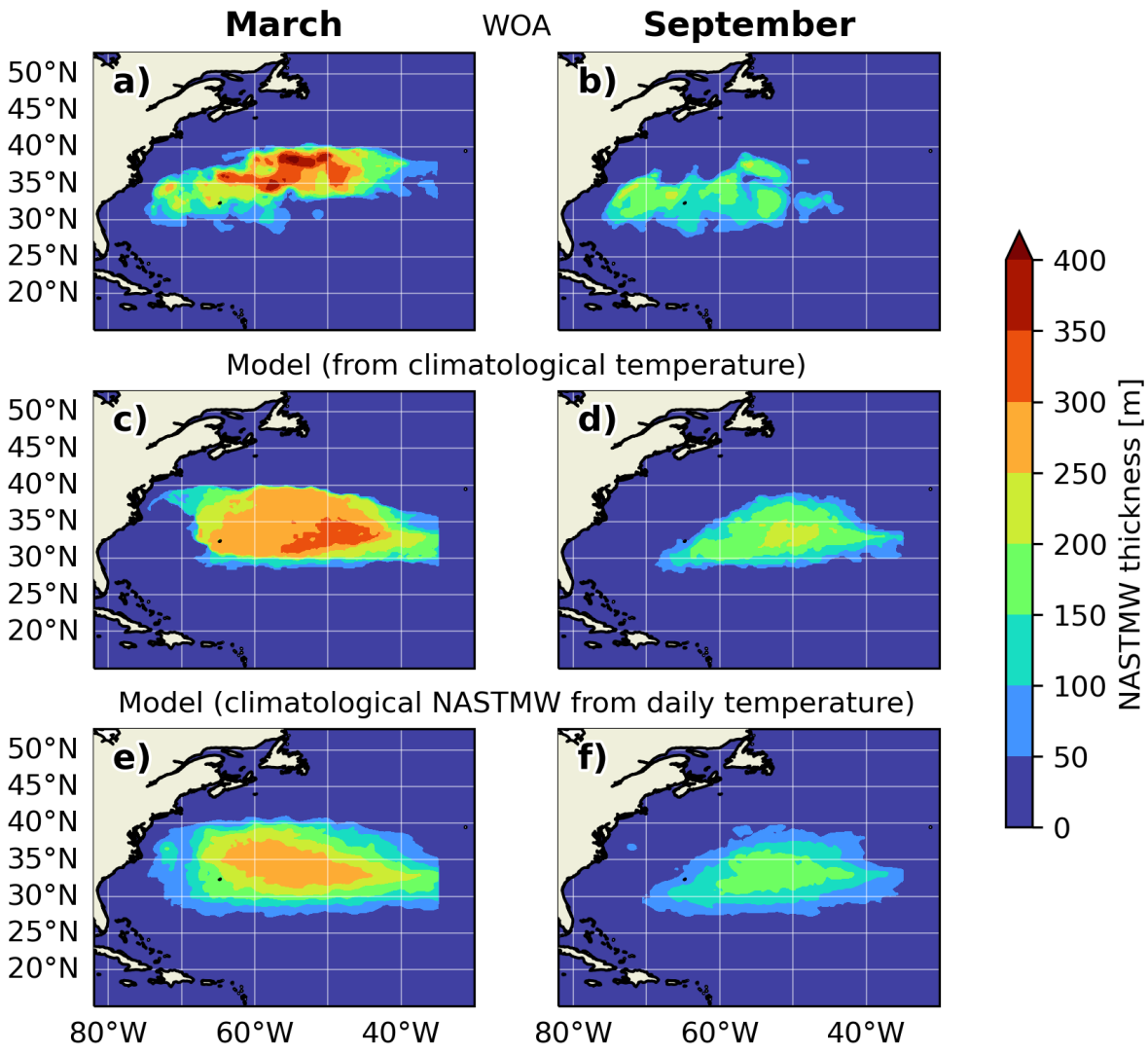

Figure S8. March and September NASTMW thickness computed using (a, b) WOA23 temperatures (1991-2020), and (c, d) climatological temperatures in FREEGLORYS2V4 (1995-2017). (e, f) Climatology of NASTMW computed from daily temperatures in FREEGLORYS2V4.

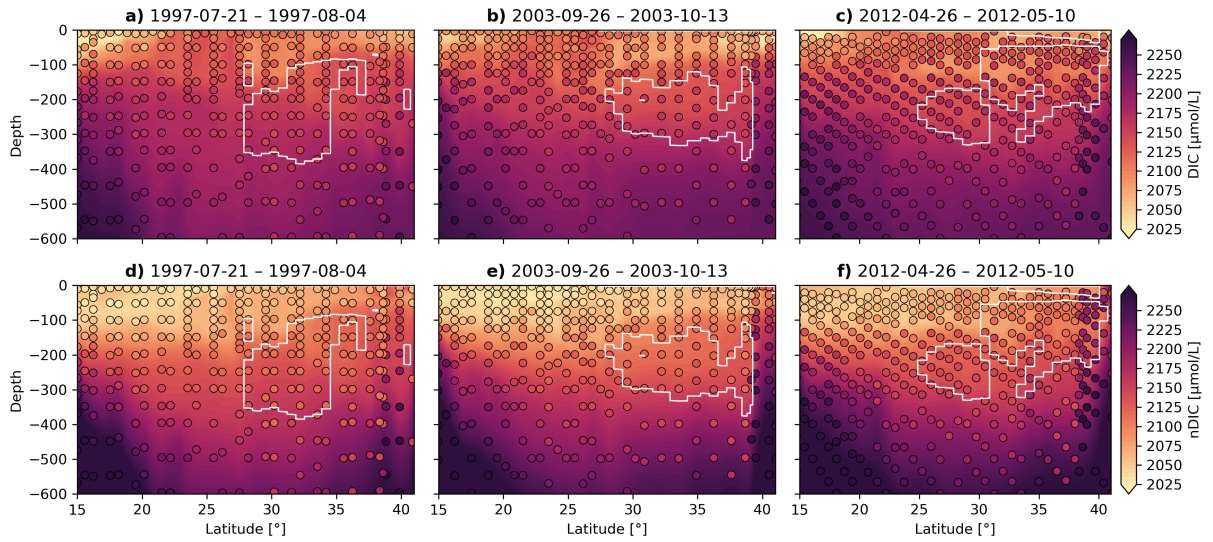

Figure S9. (a–c) Modeled and observed DIC concentrations along the A20 section. Modeled concentrations are plotted as a background field. Observations are plotted using colored dots. Model DIC snapshots are taken at (a) 28 July 1997, (b) 3 October 2003, and (c) 2 May 2012. (d–f) Salinity-normalized DIC (nDIC) for the same dates. White contours indicate two of the NASTMW constraints in the modeled data: $17\,^{\circ}\mathrm{C} < T < 20.5\,^{\circ}\mathrm{C}$ and $\partial T/\partial z < 0.01\,^{\circ}\mathrm{C\,m^{-1}}$.

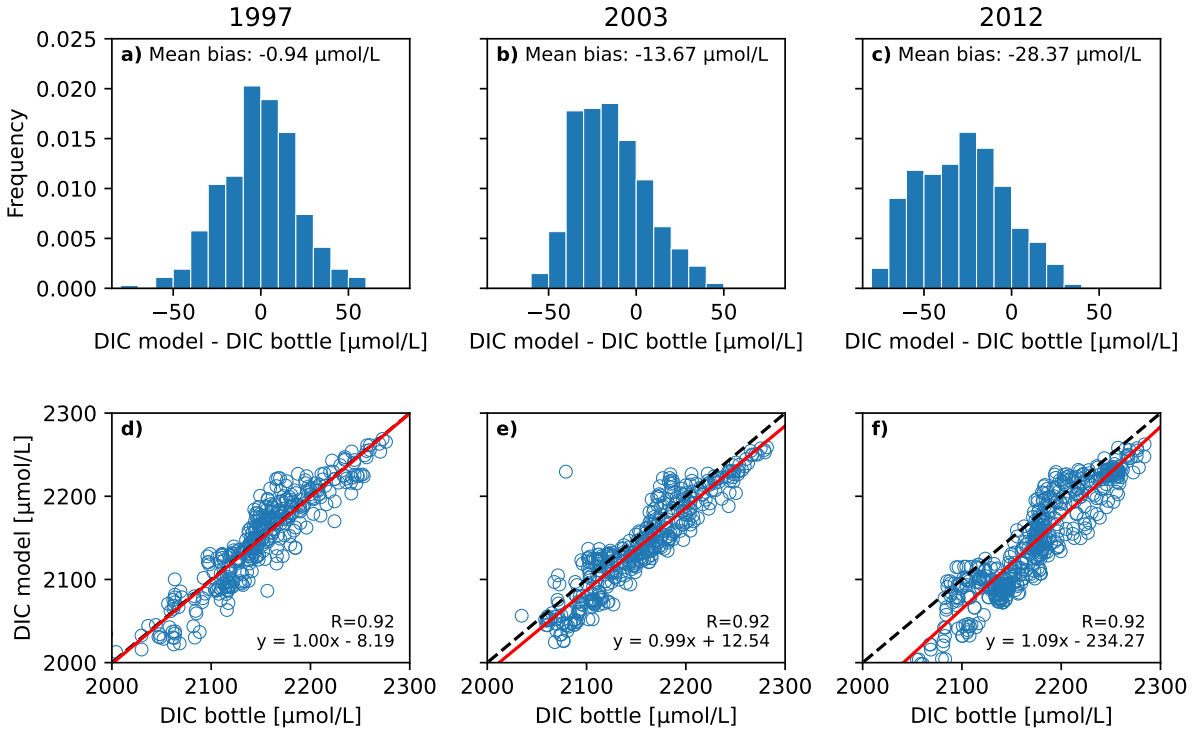

Figure S10. (a–c) Histograms with the difference in DIC between modeled and bottle DIC concentrations for each A20 transect year. Each observation is matched with the model DIC snapshot at the date and location of observation. (d–f) Scatter plot comparing observed and modeled DIC, including linear regression. R is the Pearson correlation coefficient.

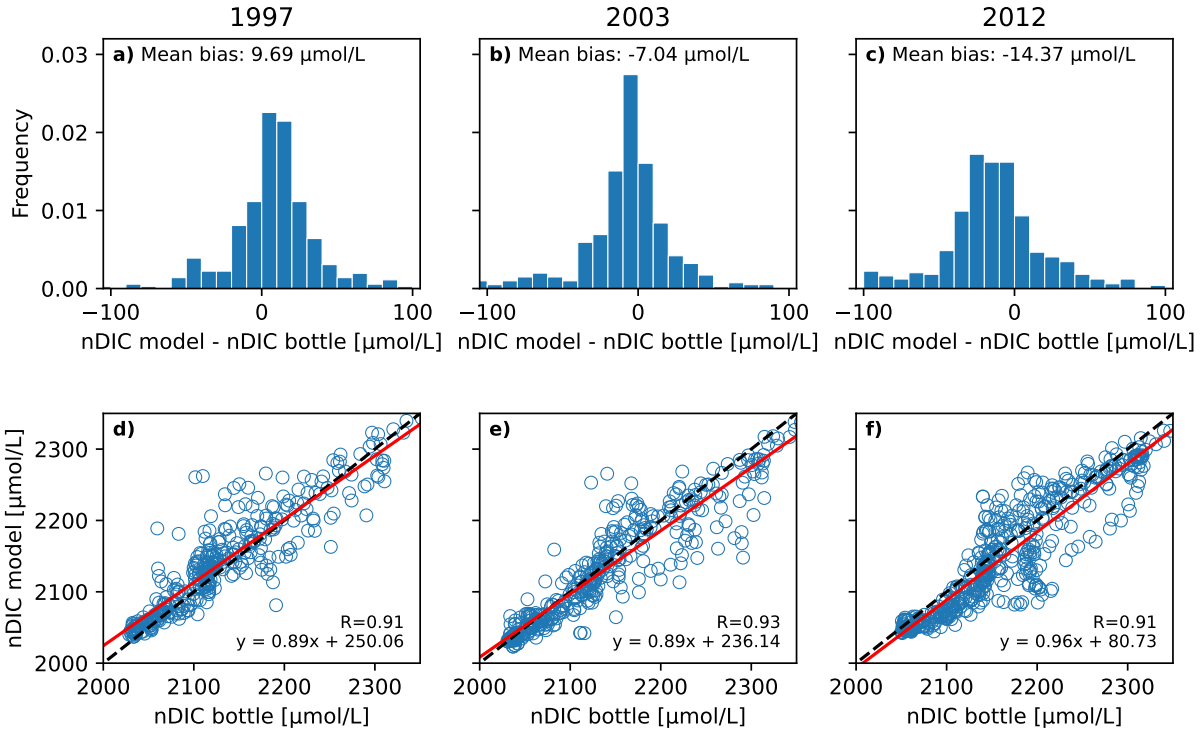

Figure S11. (a–c) Histograms with the difference in nDIC between modeled and bottle nDIC concentrations for each A20 transect year. Each observation is matched with the model nDIC snapshot at the date and location of observation. (d–f) Scatter plot comparing observed and modeled nDIC, including linear regression. R is the Pearson correlation coefficient.

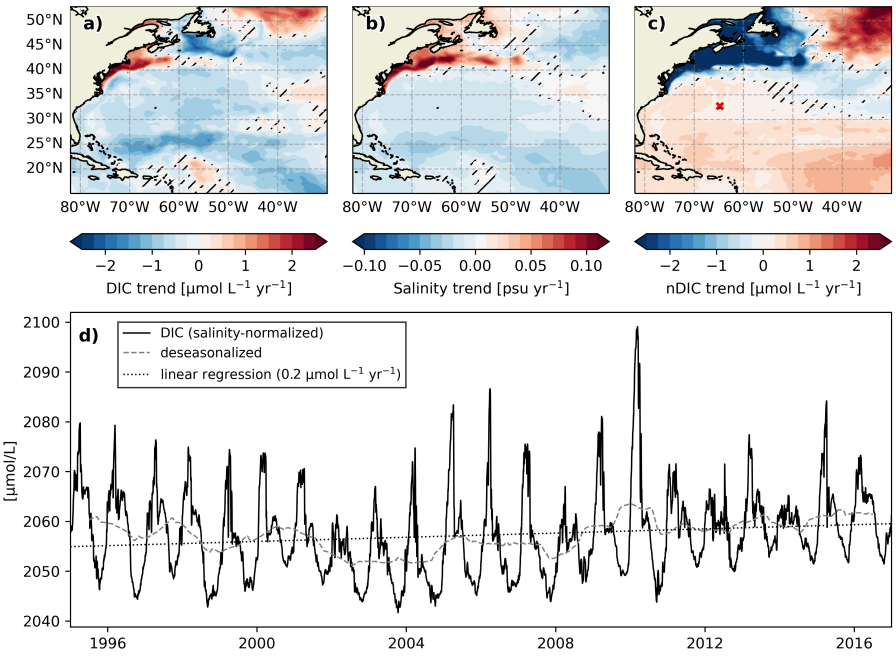

Figure S12. (a-c) Model trends between 1995 and 2017 at 10 m depth for (a) DIC, (b) salinity, and (c) nDIC. Hatched areas indicate trends that are not statistically significant ($p > 0.05$). (d) Modeled nDIC concentration at 10 m depth at 32°42′ N, 64°46′ W, close to the BATS site (red X in (c)). All trends are computed after deseasonalization based on moving averages.

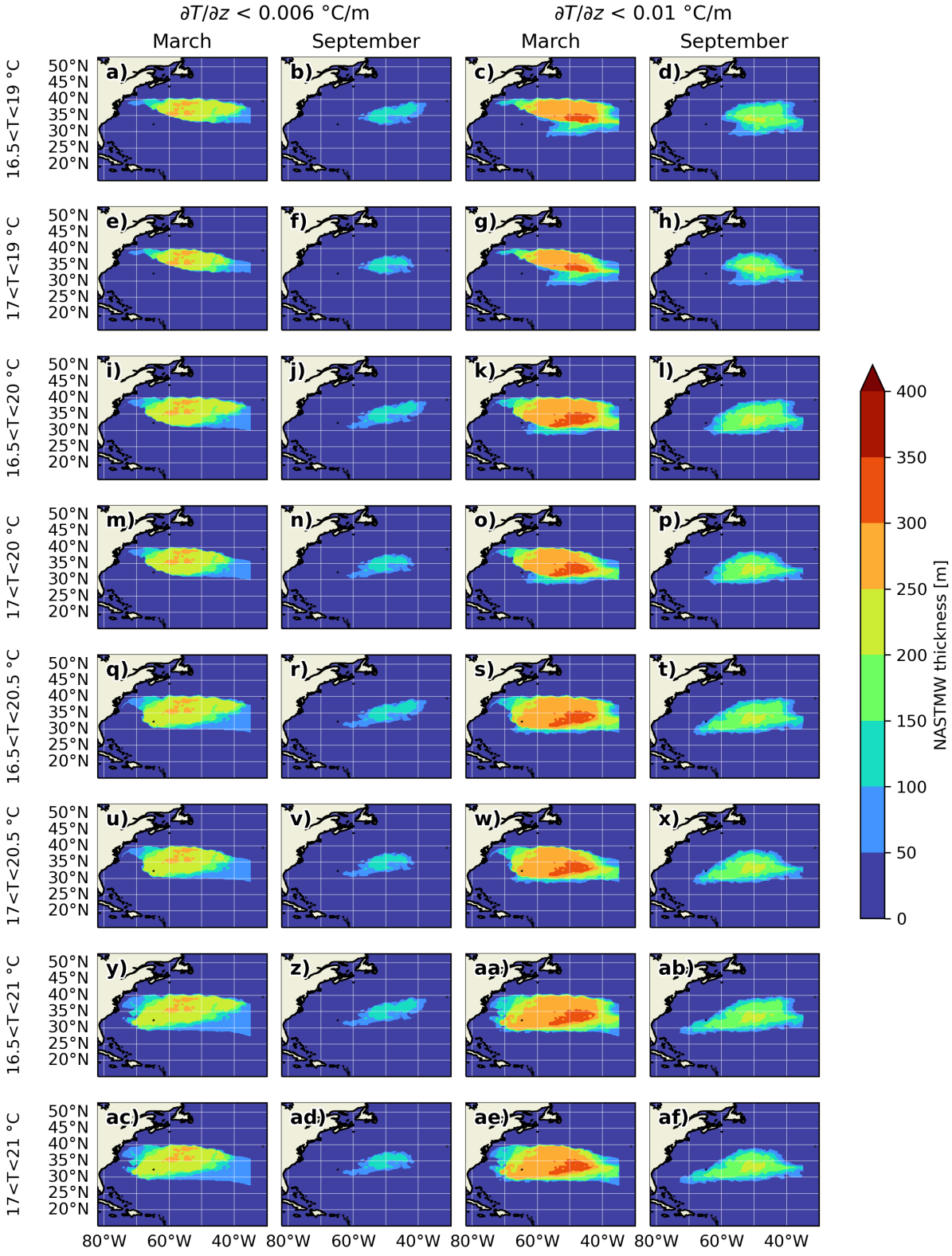

Figure S13. Model NASTMW thicknesses in March and September for different temperature and stratifications limits.

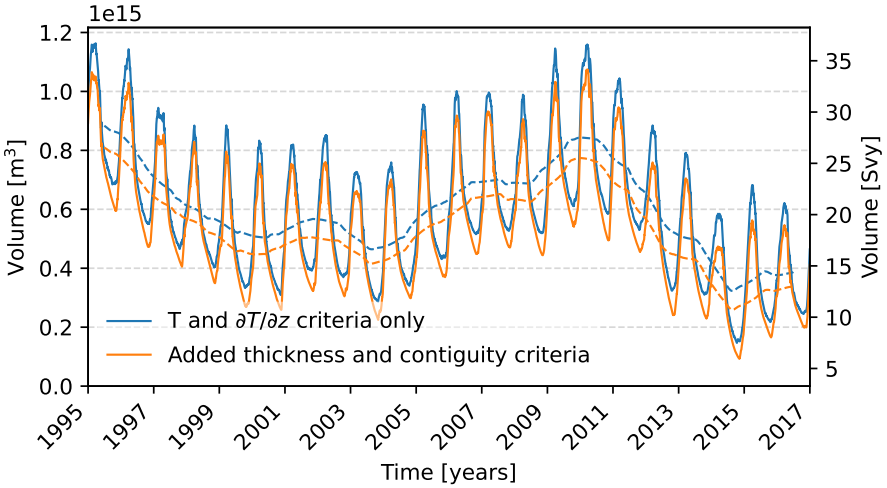

Figure S14. Modeled NASTMW volume with the definition criteria from section 2.2 of the main text. Dashed lines represent yearly averages.

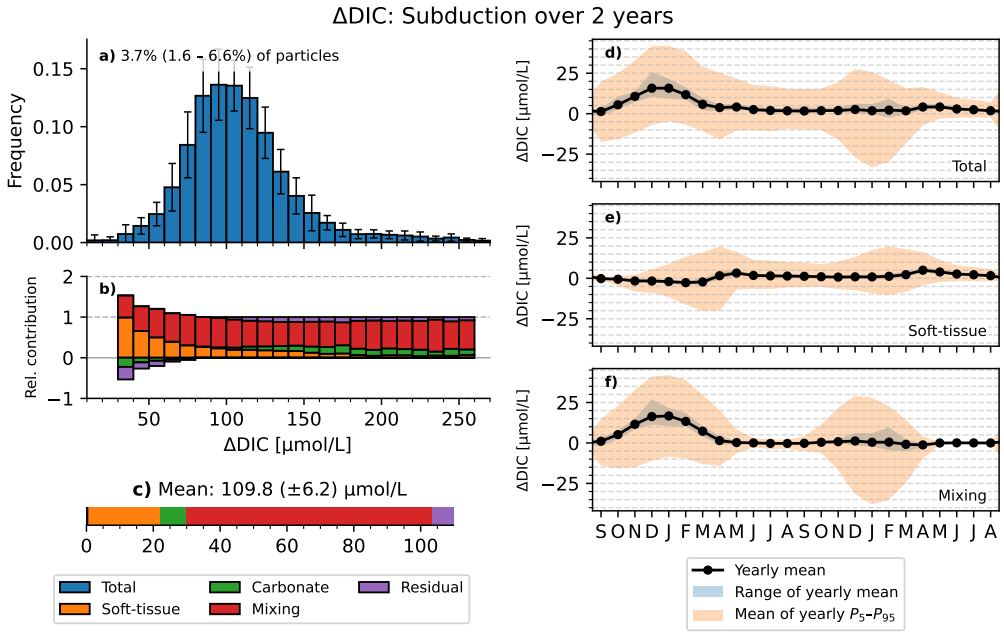

Figure S15. Transformation of DIC concentrations along pathways of subducting NASTMW parcels (allowing subduction to take place over the course of 2 years). (a) Distribution of total ΔDIC per trajectory, averaged over initialization years 1996-2015. (b) Relative contribution of each process to the average ΔDIC, for different ΔDIC strengths. (c) Mean of yearly average ΔDIC of all trajectories. (d-f) yearly mean DIC flux, integrated per month, for the total DIC flux (d), soft-tissue fluxes (e), and mixing fluxes (f).

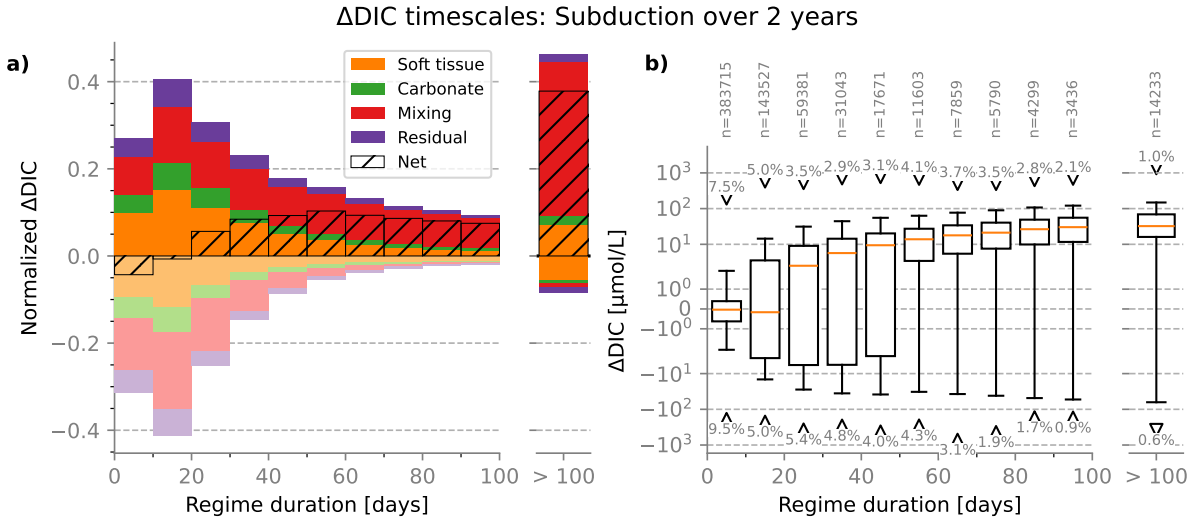

Figure S16. ΔDIC contribution of each timescale for subducting NASTMW parcels (allowing subduction to take place over the course of 2 years). (a) Relative ΔDIC of regimes of each timescale. (b) Boxplot of magnitudes of each regime for each timescale.

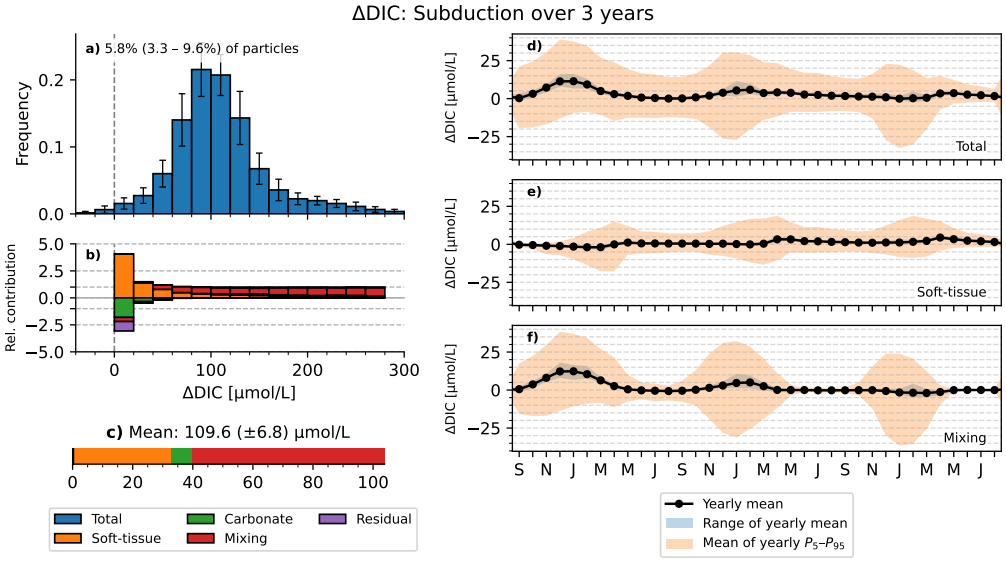

Figure S17. Transformation of DIC concentrations along pathways of subducting NASTMW parcels (allowing subduction to take place over the course of 3 years). (a) Distribution of total ΔDIC per trajectory, averaged over initialization years 1996-2015. (b) Relative contribution of each process to the average ΔDIC, for different ΔDIC strengths. (c) Mean of yearly average ΔDIC of all trajectories. (d-f) yearly mean DIC flux, integrated per month, for the total DIC flux (d), soft-tissue fluxes (e), and mixing fluxes (f).

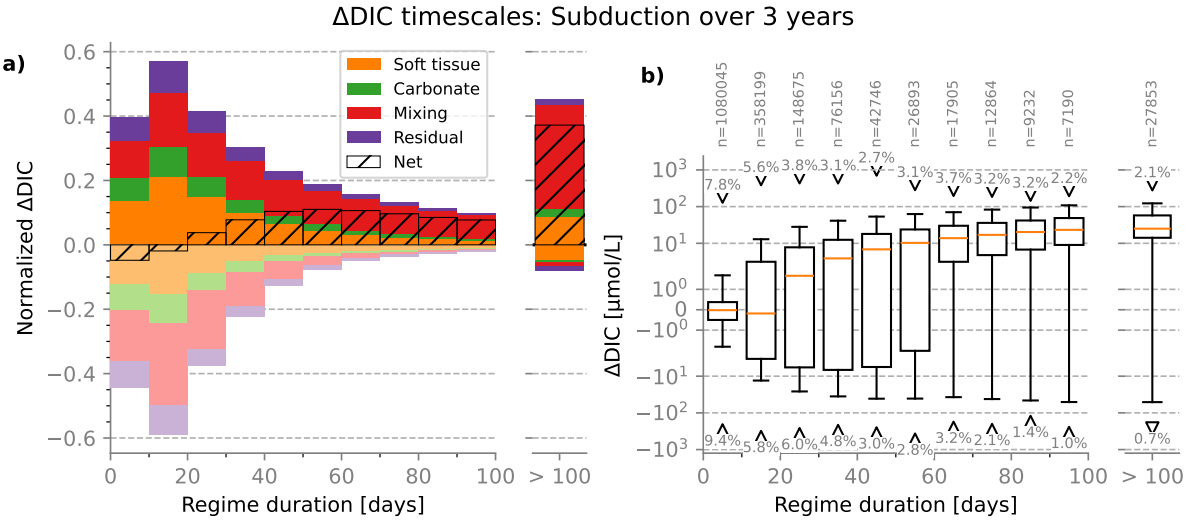

Figure S18. ΔDIC contribution of each timescale for subducting NASTMW parcels (allowing subduction to take place over the course of 3 years). (a) Relative ΔDIC of regimes of each timescale. (b) Boxplot of magnitudes of each regime for each timescale.

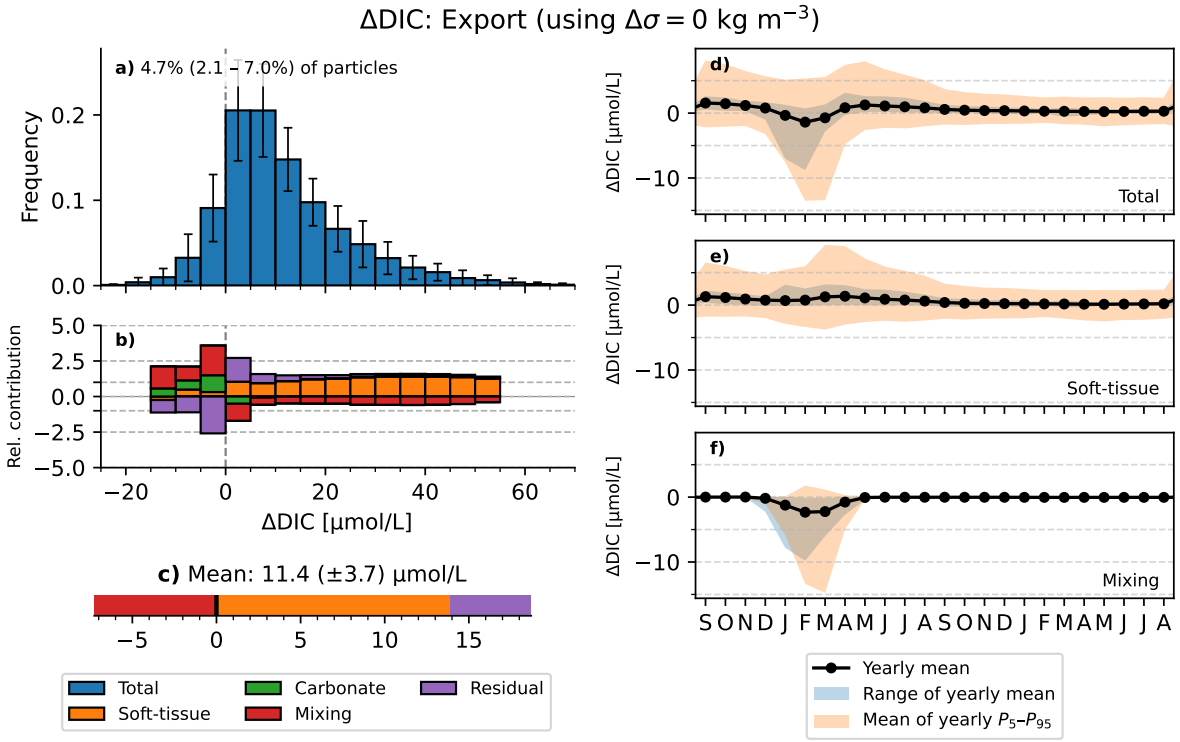

Figure S19. Transformation of DIC concentrations along pathways of exported NASTMW parcels, for $\Delta\sigma = 0\,\mathrm{kg\,m^{-3}}$. (a) Distribution of total ΔDIC per trajectory, averaged over initialization years 1995-2015. (b) Relative contribution of each process to the average ΔDIC, for different ΔDIC strengths. (c) Mean of yearly average ΔDIC of all trajectories. (d-f) yearly mean DIC flux, integrated per month, for the total DIC flux (d), soft-tissue fluxes (e), and mixing fluxes (f).

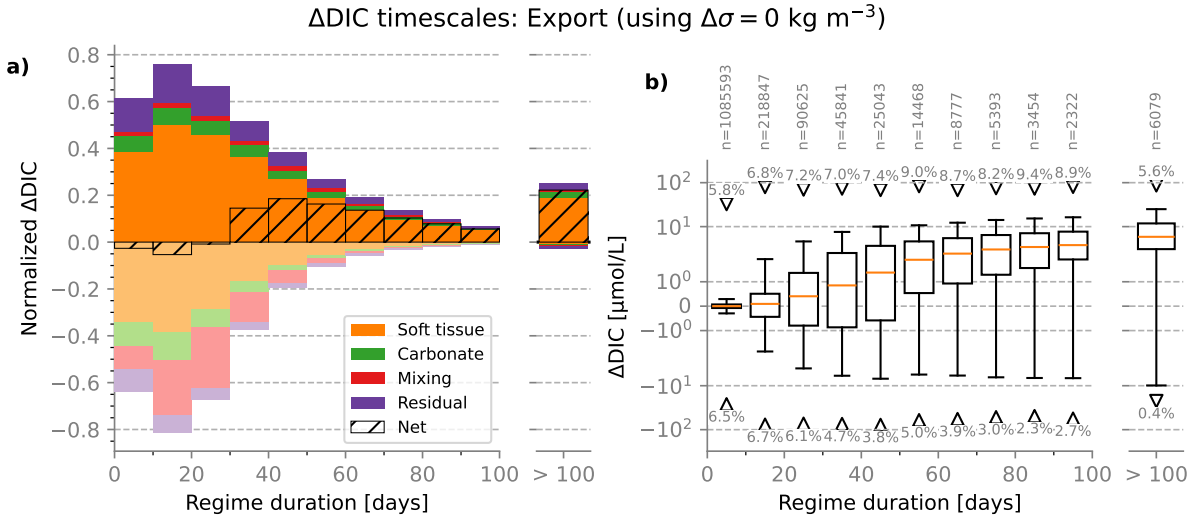

Figure S20. ΔDIC contribution of each timescale for exported NASTMW parcels for $\Delta\sigma = 0\,\mathrm{kg\,m^{-3}}$. (a) Relative ΔDIC of regimes of each timescale. (b) Boxplot of magnitudes of each regime for each timescale.

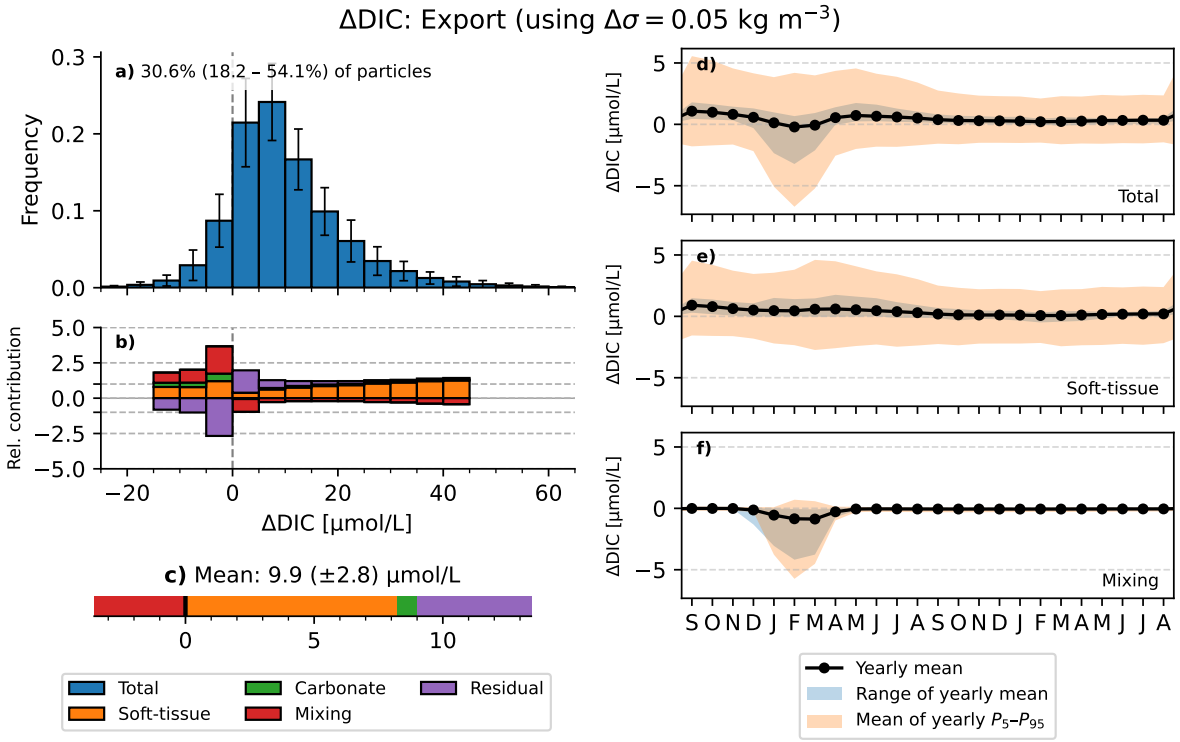

Figure S21. Transformation of DIC concentrations along pathways of exported NASTMW parcels for $\Delta\sigma = 0.05\,\mathrm{kg\,m^{-3}}$. (a) Distribution of total ΔDIC per trajectory, averaged over initialization years 1995-2015. (b) Relative contribution of each process to the average ΔDIC, for different ΔDIC strengths. (c) Mean of yearly average ΔDIC of all trajectories. (d-f) yearly mean DIC flux, integrated per month, for the total DIC flux (d), soft-tissue fluxes (e), and mixing fluxes (f).

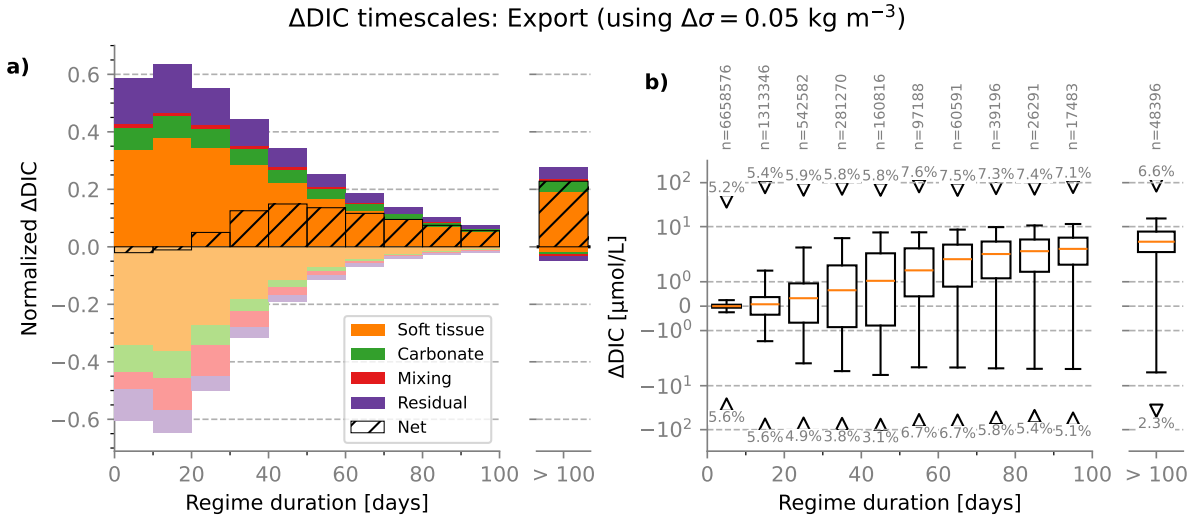

Figure S22. ΔDIC contribution of each timescale for exported NASTMW parcels, for $\Delta\sigma = 0.05\,\mathrm{kg\,m^{-3}}$. (a) Relative ΔDIC of regimes of each timescale. (b) Boxplot of magnitudes of each regime for each timescale.

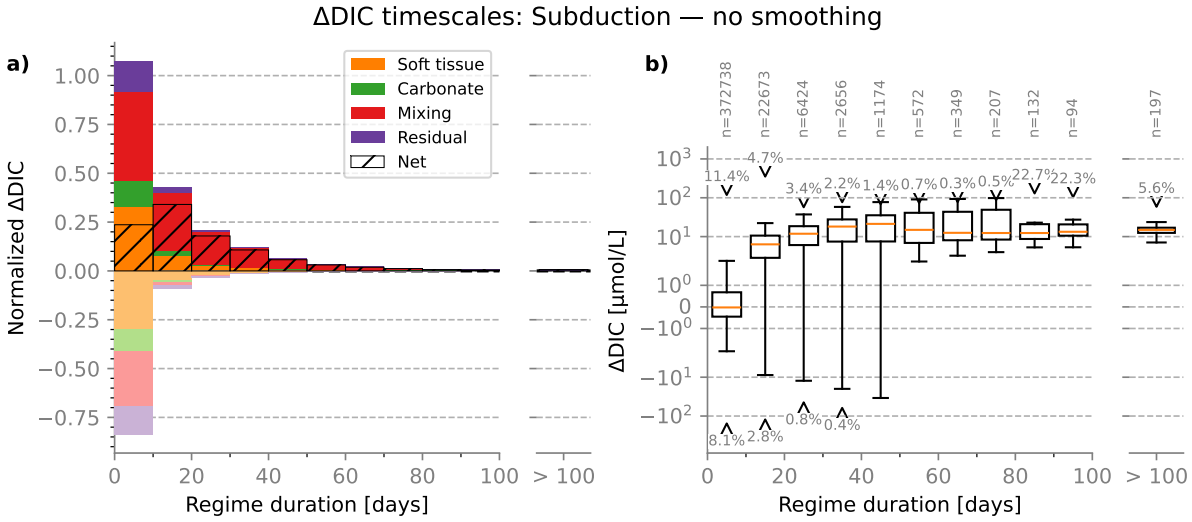

Figure S23. ΔDIC contribution of each timescale for subducting NASTMW parcels, found without applying a smoothing window. (a) Relative ΔDIC of regimes of each timescale. (b) Boxplot of magnitudes of each regime for each timescale.

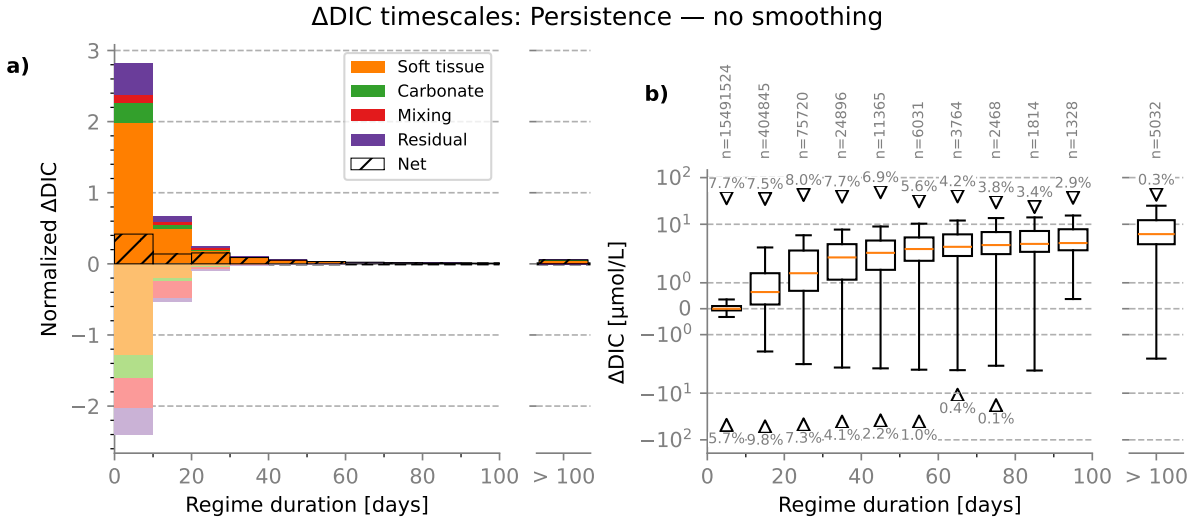

Figure S24. ΔDIC contribution of each timescale for persisting NASTMW parcels, found without applying a smoothing window. (a) Relative ΔDIC of regimes of each timescale. (b) Boxplot of magnitudes of each regime for each timescale.

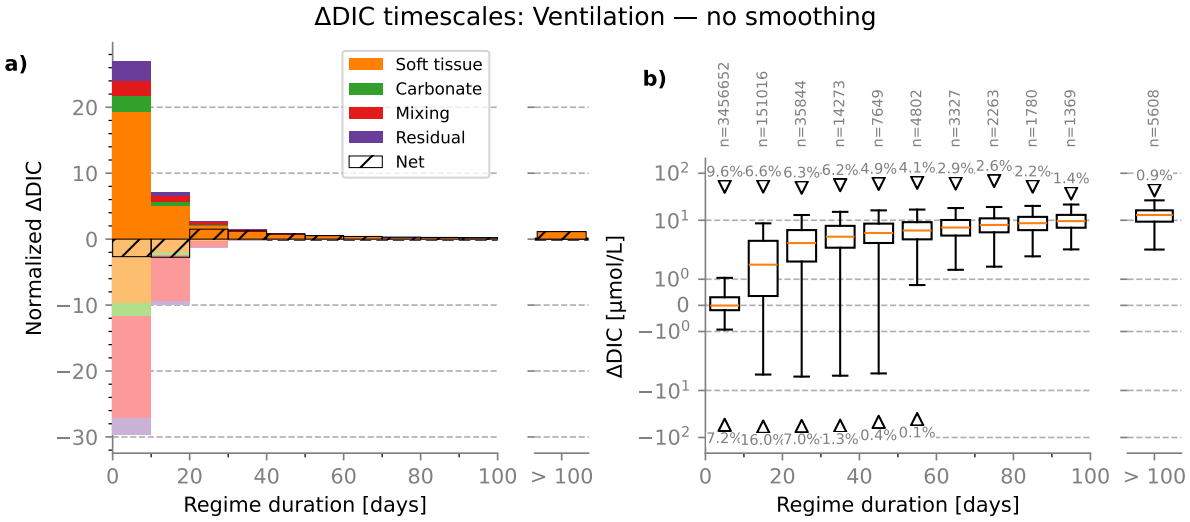

Figure S25. ΔDIC contribution of each timescale for ventilating NASTMW parcels, found without applying a smoothing window. (a) Relative ΔDIC of regimes of each timescale. (b) Boxplot of magnitudes of each regime for each timescale.

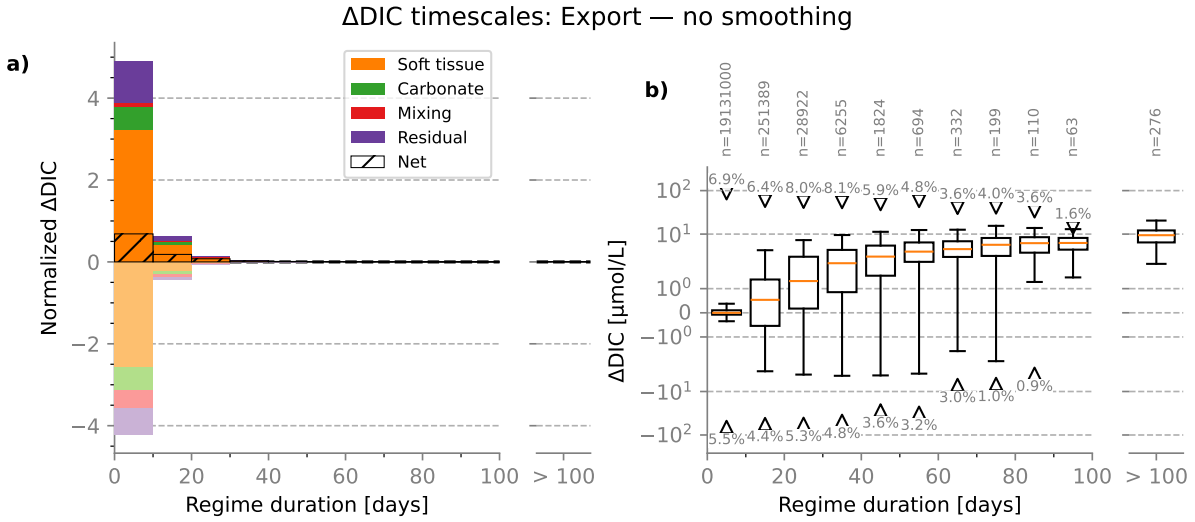

Figure S26. ΔDIC contribution of each timescale for exporting NASTMW parcels, found without applying a smoothing window. (a) Relative ΔDIC of regimes of each timescale. (b) Boxplot of magnitudes of each regime for each timescale.

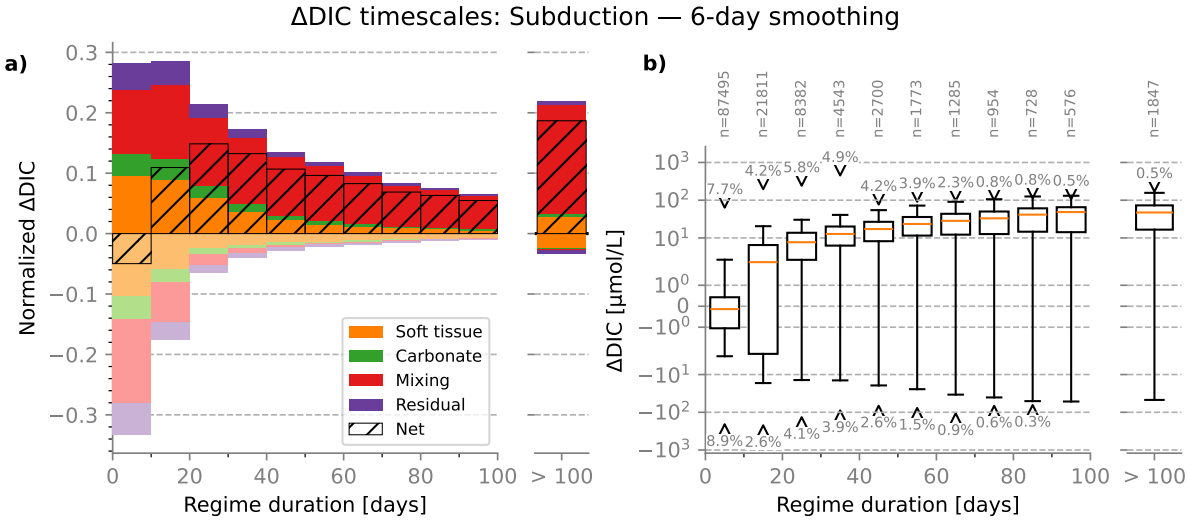

Figure S27. ΔDIC contribution of each timescale for subducting NASTMW parcels, found when applying a 6-day smoothing window. (a) Relative ΔDIC of regimes of each timescale. (b) Boxplot of magnitudes of each regime for each timescale.

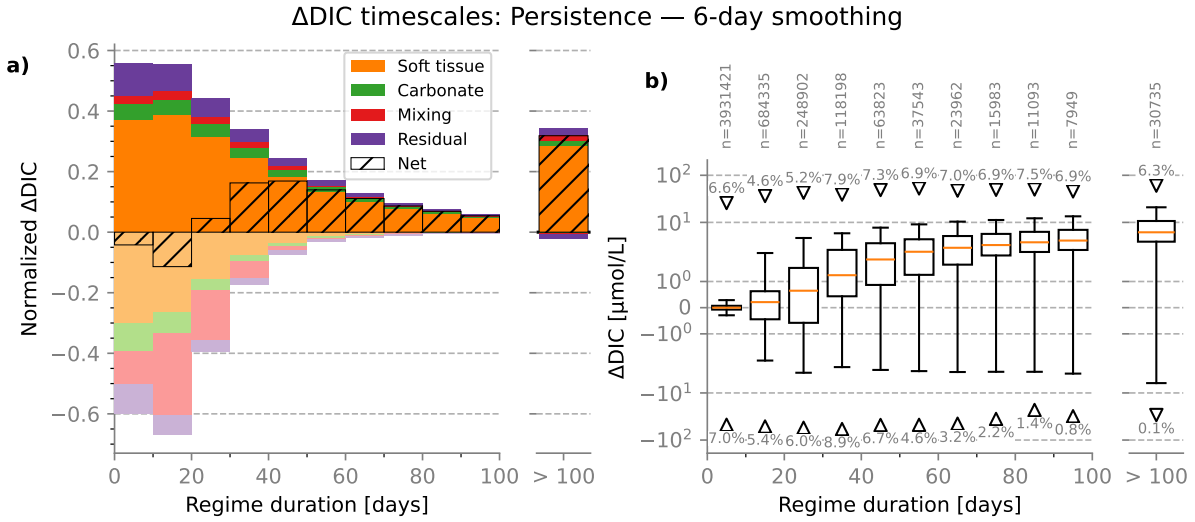

Figure S28. ΔDIC contribution of each timescale for persisting NASTMW parcels, found when applying a 6-day smoothing window. (a) Relative ΔDIC of regimes of each timescale. (b) Boxplot of magnitudes of each regime for each timescale.

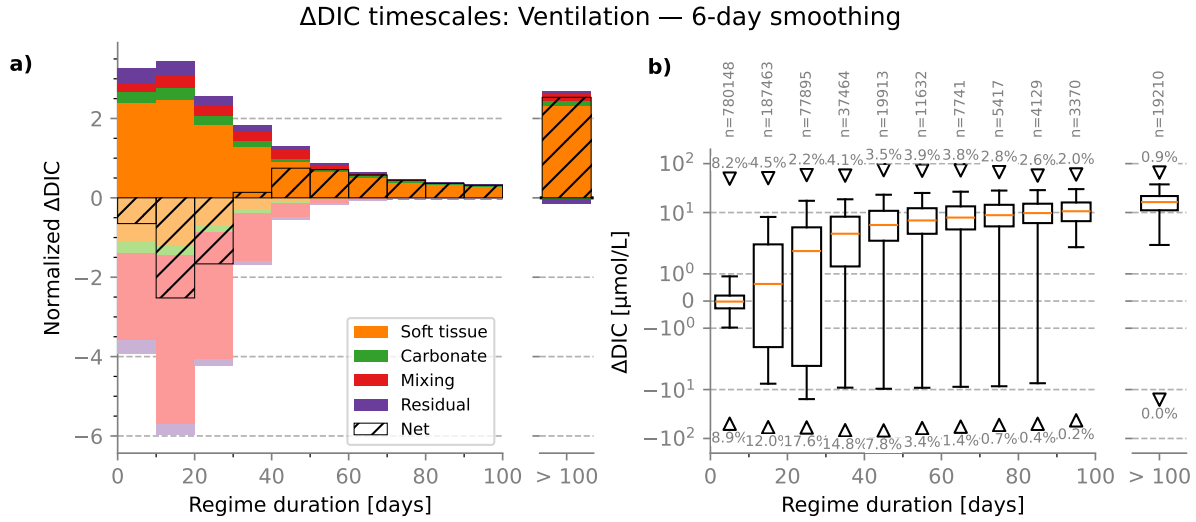

Figure S29. ΔDIC contribution of each timescale for ventilating NASTMW parcels, found when applying a 6-day smoothing window. (a) Relative ΔDIC of regimes of each timescale. (b) Boxplot of magnitudes of each regime for each timescale.

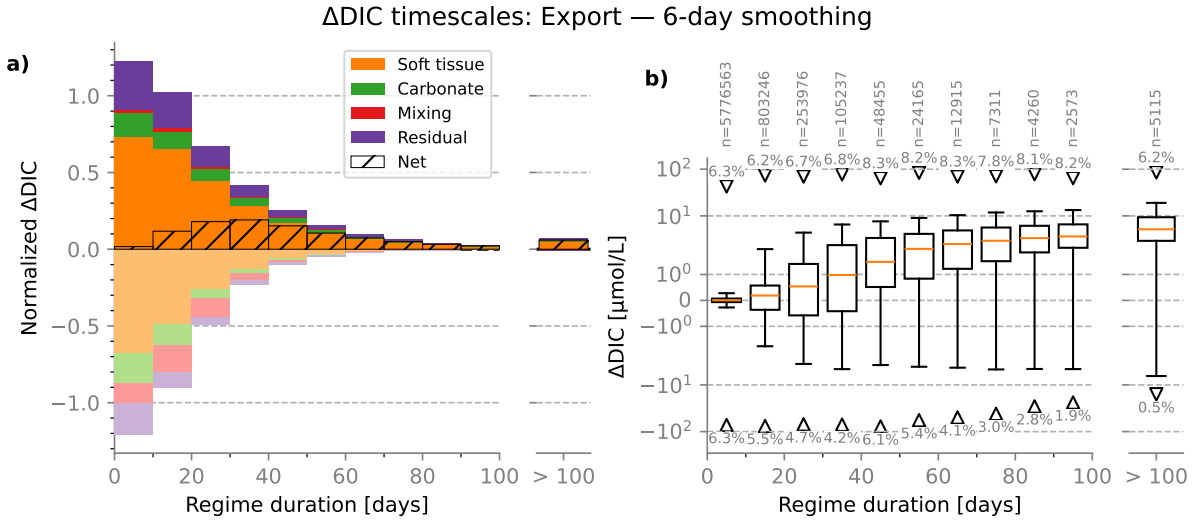

Figure S30. ΔDIC contribution of each timescale for exporting NASTMW parcels, found when applying a 6-day smoothing window. (a) Relative ΔDIC of regimes of each timescale. (b) Boxplot of magnitudes of each regime for each timescale.

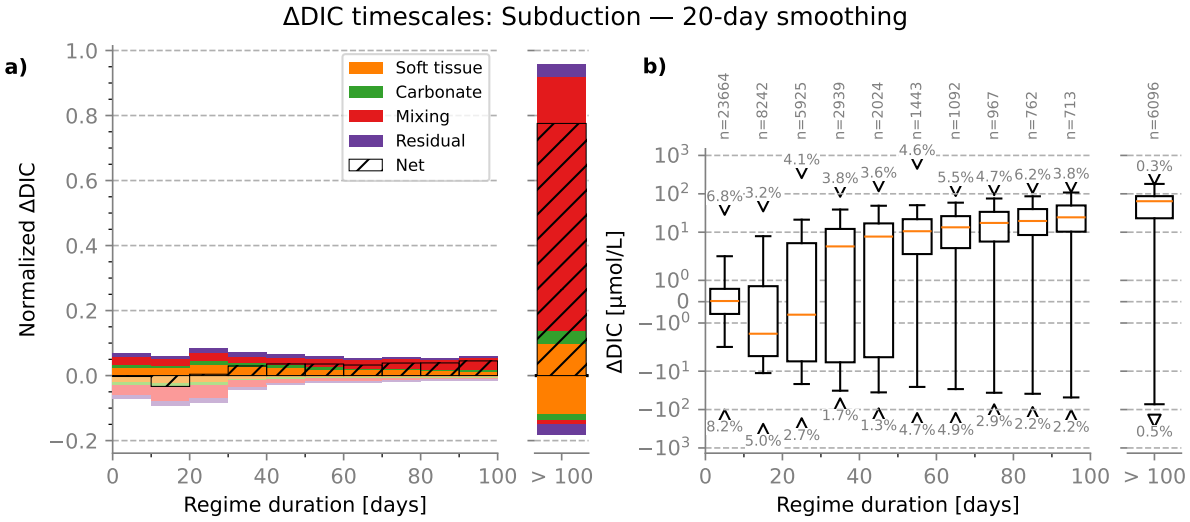

Figure S31. ΔDIC contribution of each timescale for subducting NASTMW parcels, found when applying a 20-day smoothing window. (a) Relative ΔDIC of regimes of each timescale. (b) Boxplot of magnitudes of each regime for each timescale.

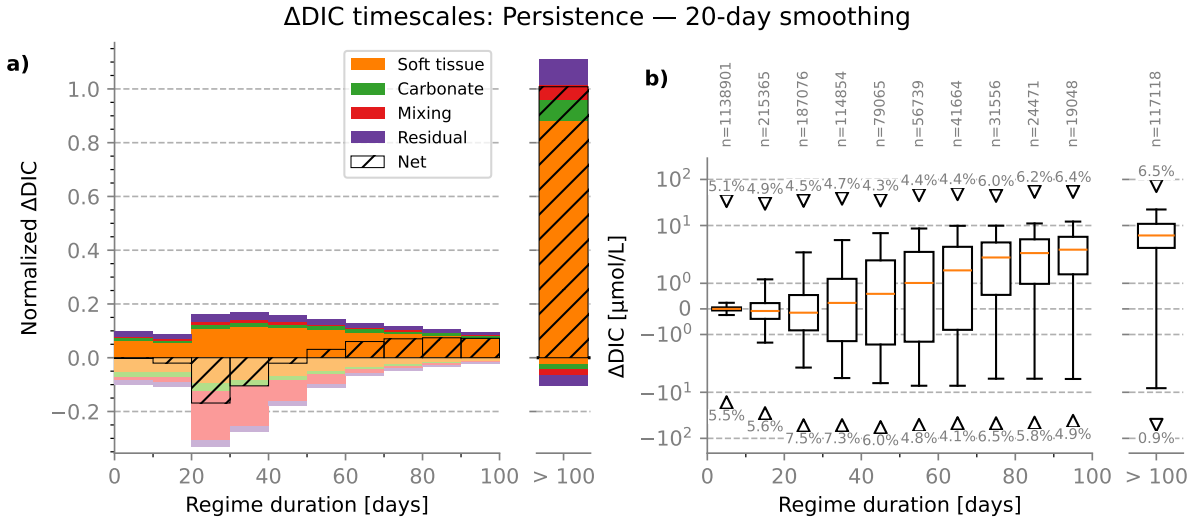

Figure S32. ΔDIC contribution of each timescale for persisting NASTMW parcels, found when applying a 20-day smoothing window. (a) Relative ΔDIC of regimes of each timescale. (b) Boxplot of magnitudes of each regime for each timescale.

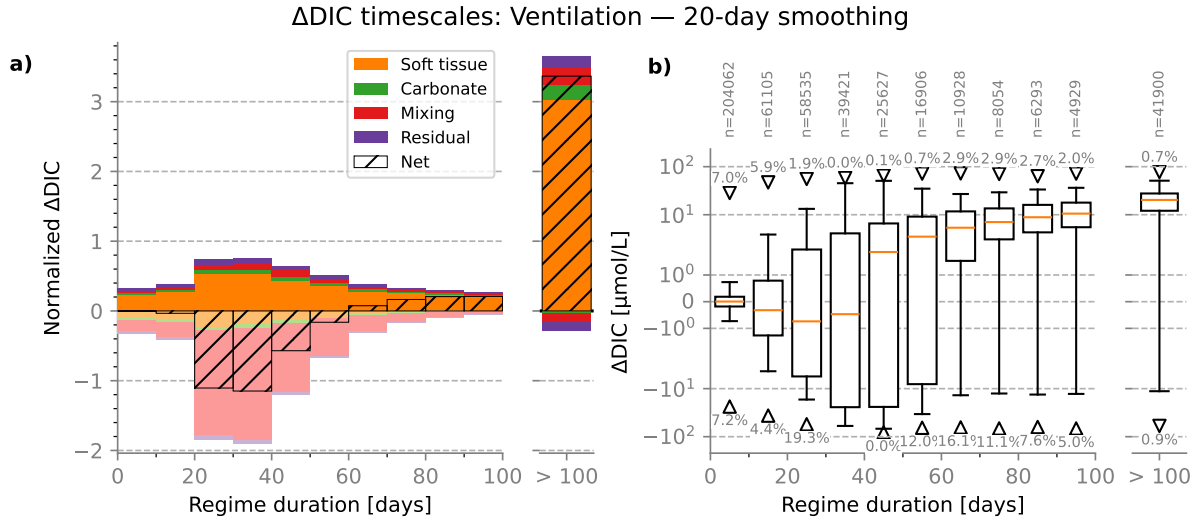

Figure S33. ΔDIC contribution of each timescale for ventilating NASTMW parcels, found when applying a 20-day smoothing window. (a) Relative ΔDIC of regimes of each timescale. (b) Boxplot of magnitudes of each regime for each timescale.

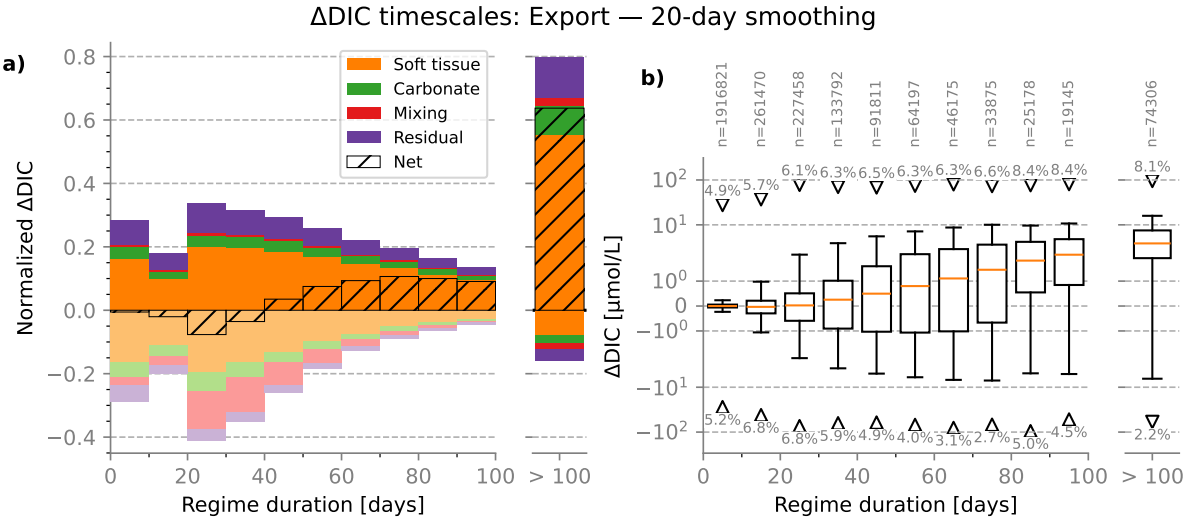

Figure S34. ΔDIC contribution of each timescale for exporting NASTMW parcels, found when applying a 20-day smoothing window. (a) Relative ΔDIC of regimes of each timescale. (b) Boxplot of magnitudes of each regime for each timescale.

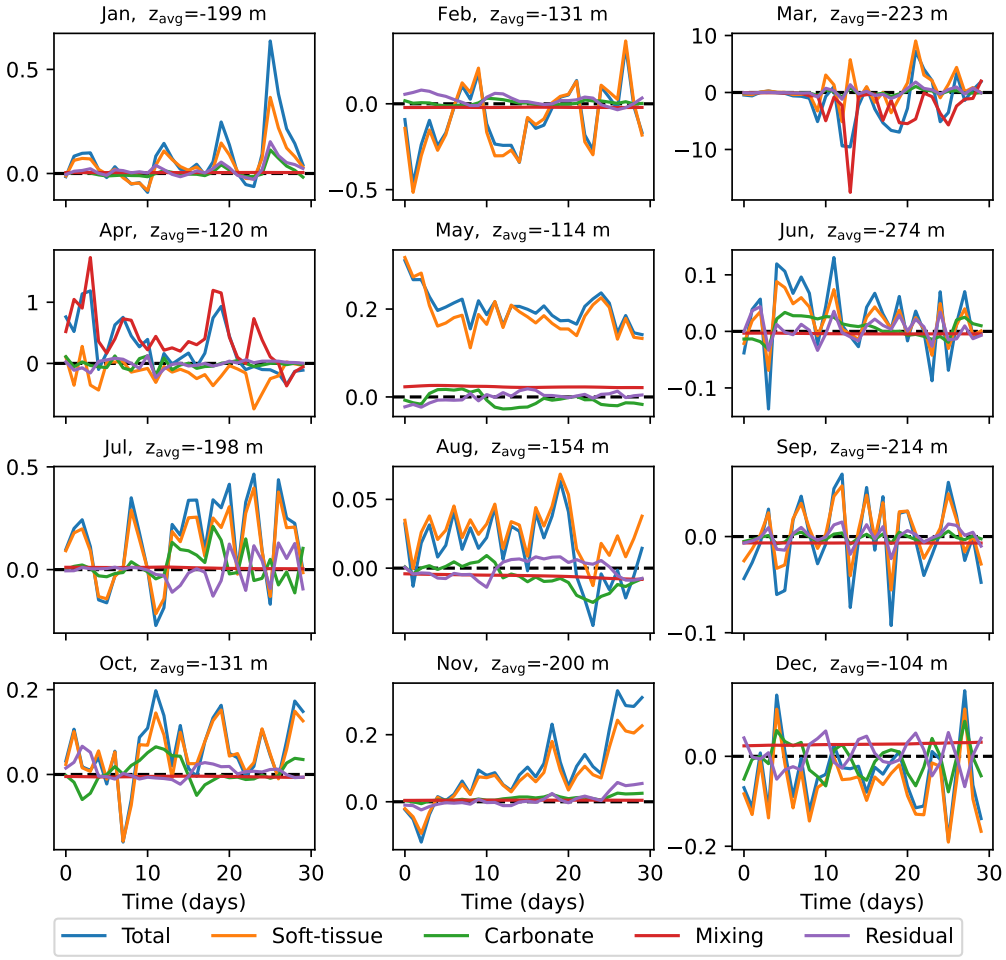

Figure S35. Daily DIC fluxes [µmol L^{-1} d^{-1}] for 12 random trajectories in 12 months, from parcels that were initialized in September 2000. The soft-tissue flux often dominates the signal, while the mixing flux is mainly relevant in when the particle is in the mixing layer.

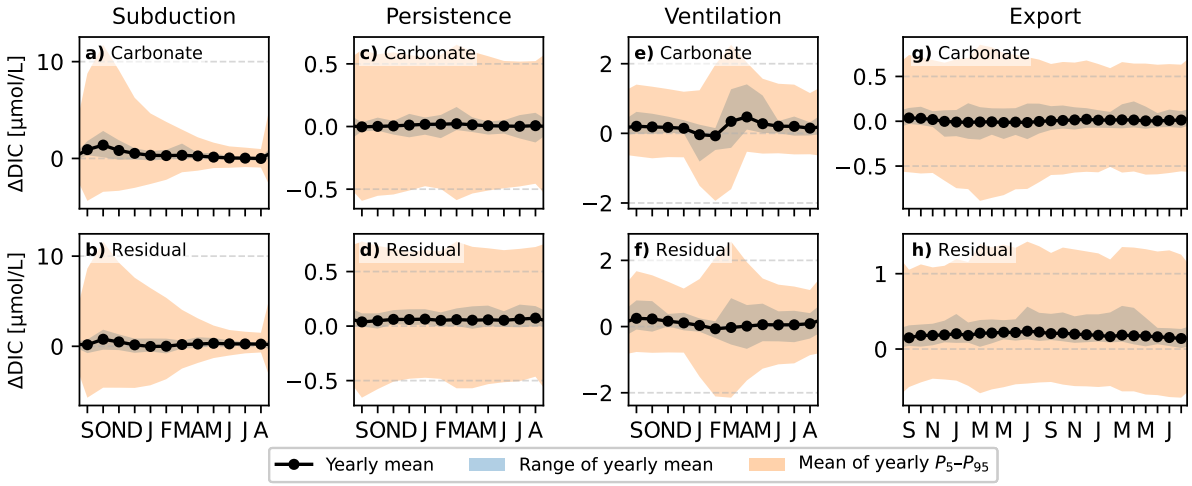

Figure S36. Yearly mean DIC fluxes for carbonate and residual processes, integrated per month, as well as the range of the yearly mean, and the mean of the 5th and 95th percentile for the four NASTMW pathways discussed in the main text: (a, b) subduction, (c, d) persistence, (e, f) ventilation, and (g, h) export.

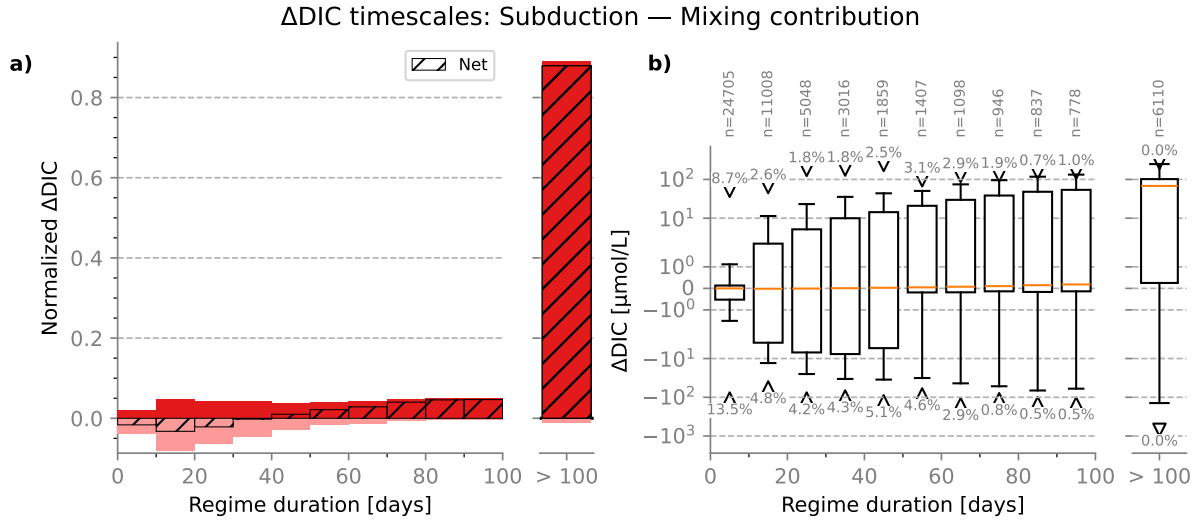

Figure S37. ΔDIC contribution of each timescale for subducting NASTMW based on DIC anomalies from mixing processes. (a) Relative ΔDIC of regimes of each timescale. (b) Boxplot of magnitudes of each regime for each timescale.

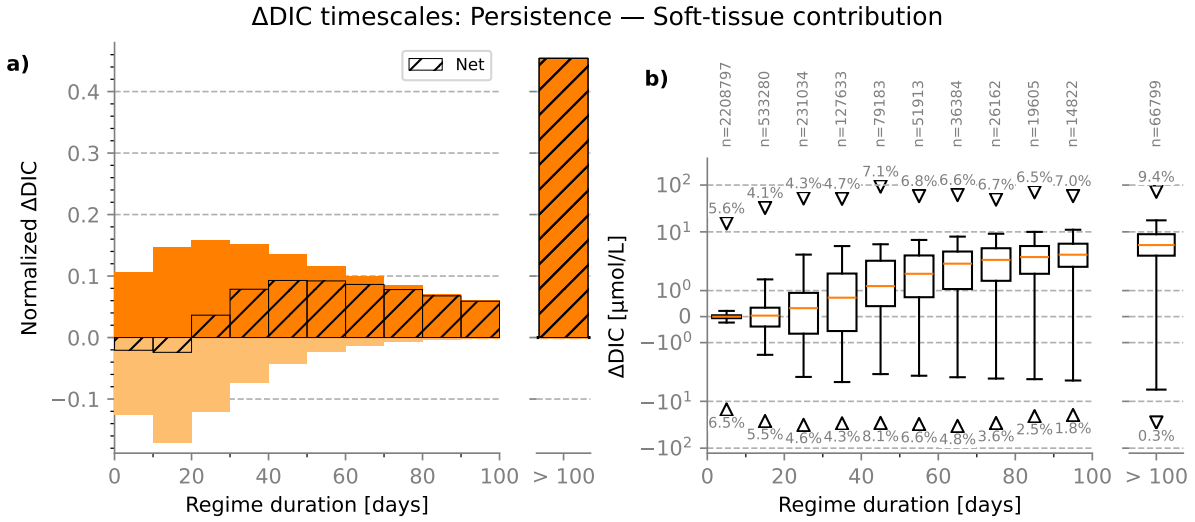

Figure S38. ΔDIC contribution of each timescale for parcels persisting in NASTMW, based on DIC anomalies from soft-tissue processes. (a) Relative ΔDIC of regimes of each timescale. (b) Boxplot of magnitudes of each regime for each timescale.

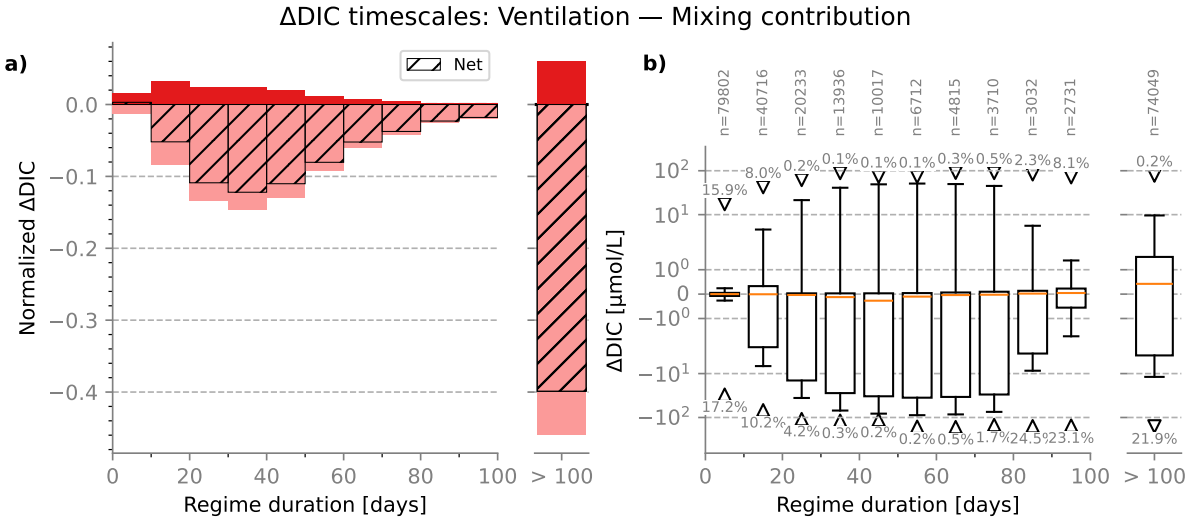

Figure S39. ΔDIC contribution of each timescale for ventilating NASTMW based on DIC anomalies from mixing processes. (a) Relative ΔDIC of regimes of each timescale. (b) Boxplot of magnitudes of each regime for each timescale.